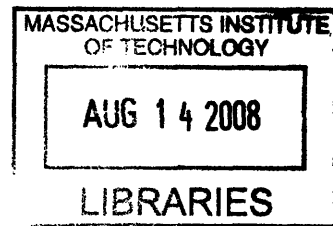


Influence of Electrode Stress on Proton Exchange Membrane Fuel Cell Performance:  
Experimental Characterization and Power Optimization

by

**Betar M. Gallant**



SUBMITTED TO THE DEPARTMENT OF MECHANICAL ENGINEERING IN  
PARTIAL FULFILLMENT OF THE REQUIREMENTS FOR THE DEGREE OF

BACHELOR OF SCIENCE IN MECHANICAL ENGINEERING  
AT THE  
MASSACHUSETTS INSTITUTE OF TECHNOLOGY

JUNE 2008

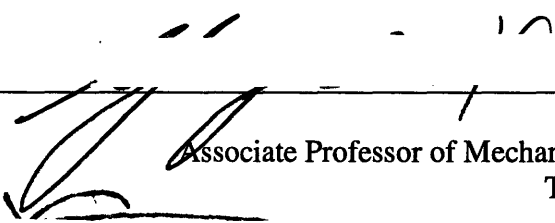
©2008 Betar M. Gallant. All rights reserved.

The author hereby grants to MIT permission to reproduce  
and to distribute publicly paper and electronic  
copies of this thesis document in whole or in part  
in any medium now known or hereafter created.

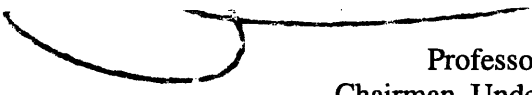
Signature of Author: \_\_\_\_\_

Department of Mechanical Engineering  
05-06-2008

Certified by: \_\_\_\_\_

  
Yang Shao-Horn  
Associate Professor of Mechanical Engineering  
Thesis Supervisor

Accepted by: \_\_\_\_\_

  
John H. Lienhard V  
Professor of Mechanical Engineering  
Chairman, Undergraduate Thesis Committee

# Influence of Electrode Stress on Proton Exchange Membrane Fuel Cell Performance: Experimental Characterization and Power Optimization

By

Betar M. Gallant

Submitted to the Department of Mechanical Engineering  
On May 06, 2008 in partial fulfillment of the  
Requirements for the Degree of Bachelor of Science in  
Mechanical Engineering

## Abstract

Compressive stress applied to the electrode area of a Proton Exchange Membrane (PEM) fuel cell is known to significantly affect power output. In practice, electrode stress arises during operation due to the clamping force that is necessary for sealing the cell. In traditional fuel cell designs, the sealing requirement and the clamping stress are inherently coupled and it is difficult to experimentally determine the magnitude of stress experienced by the electrodes. Investigations of the stress-performance relationship in the literature have not addressed this inherent coupling and it is uncertain whether prior stress measurement techniques are accurate.

In order to address the limitations of a traditional fuel cell design in applying and measuring electrode stress, a new test setup was designed by the author in which electrode stress and sealing requirements are decoupled and applied stress is constrained to the electrode area only. This test setup allows for accurate description of the stress-dependent cell performance as a function of different operating and engineering parameters. Data collected using this test setup can be used to optimize PEM fuel cell performance through consideration of the inherent coupling between parameters and their effect on power output.

Performance data as a function of applied stress were obtained using the new setup for a range of cell temperatures and inlet gas pressures. In general, the peak power density was found to increase rapidly at low applied stress (below 1.6 MPa) and to level off near 4.0 MPa. Changing the cell backpressure from 0 psi to 10 psi and then 20 psi improved the power density at high stress but did not help performance below 1.6 MPa. Cell operation at 45°C yielded a power density that was 28% higher than at 23°C, but a further increase to 65°C caused cell performance to decline at all values of applied stress. Overall, increasing the applied stress from 0.8 MPa to 4.4 MPa resulted in an increase in the cell power density by a factor of 2-3 for all operating conditions and had a greater effect on cell performance than did changing the backpressure or cell temperature.

Thesis Supervisor: Yang Shao-Horn

Title: Associate Professor of Mechanical Engineering

# Acknowledgements

I would first like to acknowledge my parents for their unwavering encouragement and support of my academic and personal growth. To my mother: you have taught me to be independent, persistent, and to never lose sight of the larger goals of my work. To my father: it is you whom I thank for my scientific spirit and curiosity, and I know you would be delighted to see what I have accomplished with the skills that you taught me in my younger years.

I thank Professor Yang Shao-Horn for her role as my research advisor and mentor. During our more than two years working together, you have guided and inspired my development as a researcher and ignited my passion for the electrochemical energy field. Thank you for the many great opportunities and insights along the way. Your support has been invaluable and has helped shape my experience and success at MIT. I look forward to many more years of collaboration and fun as a graduate student in your lab.

To Ethan Crumlin: You have taught me to look at problems critically and in new ways and have overseen my growth from a sophomore UROP student to a soon-to-be graduate student. Thank you for always giving me new things to learn and think about, for your insights and suggestions, and for helping me become a better researcher and engineer.

I would also like to extend a special thank you to Jacob Katz for your help as my sounding board and personal encyclopedia.





# Contents

Abstract.....	2
List of Figures.....	7
1.0 Introduction.....	11
1.1 The Energy Challenge: The Fuel Cell in Historical Context.....	11
1.2 Fuel Cells: State of the Art.....	13
1.3 Challenges for Large-Scale Implementation .....	14
2.0 Background.....	16
2.1 Fuel Cell Operating Principles.....	16
2.1.1 PEM Fuel Cell Components .....	16
2.1.2 PEM Fuel Cell Chemical Reactions .....	19
2.1.3 Open Circuit Voltage (OCV).....	21
2.1.4 Typical Voltage-Current (V-I) Curve .....	23
2.1.5 Power .....	25
2.1.6 Fuel Cell Design: Parameters that Affect Power Output.....	26
2.1.7 Expected Results of Variations in Selected Operating Parameters .....	27
2.2 PEM Fuel Cell Compression .....	28
2.2.1 Investigations in the Literature .....	29
2.2.2 Limitations of Previous Approaches.....	35
2.2.3 Questions to Answer about Fuel Cell Compression .....	37
3.0 Design and Manufacture of a Decoupled Test Setup for Studying the Stress- Performance Relationship in PEM Fuel Cells .....	39
3.1 Design Requirements for a Decoupled System .....	39
3.2 Presentation of Design .....	40
3.3 Unique Features of the Test Setup.....	45
3.4 Selection of Material and Morphological Parameters .....	47
4.0 Experimental Approach .....	50
4.1 Selection of Operating Parameters.....	50
4.2 Cell conditioning.....	50
4.3 V-I Curves.....	51
4.4 Electrochemical Impedance Spectroscopy (EIS).....	52
4.4.1 Overview: Information Gained from EIS .....	52
4.4.2 EIS for a PEM Fuel Cell .....	52
4.4.3 Use of EIS in this Study.....	55
4.5 Testing for MEA Degradation .....	56
4.6 Error Analysis .....	56
5.0 Experimental Results and Discussion.....	57
5.1 Effect of Applied Stress on PEM Fuel Cell Performance.....	57
5.2 Effect of Backpressure on Stress-Performance Relationship .....	60
5.3 Effect of Temperature on Stress-Performance Relationship .....	64
5.4 Ohmic Resistance as a Function of Stress .....	67
5.5 Performance Optimization.....	68
5.6 Use of EIS to Support Findings .....	70
6.0 Summary.....	75

7.0	Future Work and Impact .....	77
	Bibliography .....	80
	Appendix A: Additional Stress-Performance Data.....	84
	Appendix B: Effect of Cell Operation at 65°C .....	88

# List of Figures

Figure 1. Ragone plot of energy and power density comparisons between different energy conversion and storage technologies.....	14
Figure 2. The porous structure of the gas diffusion electrode (GDE) on the micro-scale allows hydrogen and oxygen to access the electrode catalyst sites [16].....	17
Figure 3. Membrane Electrode Assembly (MEA) for a PEM fuel cell [17]. The electrolyte is a thin translucent polymer and the electrodes/gas diffusion backings appear in black. ....	17
Figure 4. Graphite current collector with machined serpentine flow field in a traditional PEM fuel cell setup. ....	18
Figure 5. Fully assembled PEM fuel cell. ....	19
Figure 6. Summary of cell reactions in a PEM fuel cell. At the anode, hydrogen is oxidized into protons, which travel through the membrane, and electrons, which are forced around an external circuit. At the cathode, oxygen, protons and electrons combine to produce water [20]. ....	20
Figure 7. Typical voltage-current (V-I) and power-current (P-I) curves for a PEM fuel cell. The P-I curve is obtained from the product of voltage and current at each point along the V-I curve. ....	24
Figure 8. Contributions to the net voltage loss (overpotential) in a PEM fuel cell: activation, ohmic, and mass transport overpotentials. ....	24
Figure 9. Imaging of surface roughness of a gas diffusion layer in a PEM fuel cell [27]. ....	30
Figure 10. Surface roughness limits the surface area contact between two materials and contributes to the contact resistance across the interface [27]. ....	30
Figure 11. Comparison of force-dependent contact resistance for stainless steel grades 316L, 317L, 904L and 349 <sup>TM</sup> . Contact resistance decreases exponentially with increasing compaction force and is consistently highest for 316L [28]. ....	31
Figure 12. Dependence of contact resistance on flow-field rib width for different GDL types (a) and compaction force magnitudes (b) [29]. ....	32
Figure 13. PTFE-coated GDL in pristine form prior to compression [30]. ....	33
Figure 14. PTFE-coated GDL after being compressed for 5 minutes at (a) 0.18 MPa, (b) 0.36 MPa, (c) 0.68 MPa, and (d) 1.37 MPa. Mechanical degradation of the GDL structure is observed for all cases, particularly for (c) and (d) [30]. ....	33
Figure 15. Relative changes in interfacial resistance and porosity as a function of clamping force for two different GDLs. The interfacial resistance decreases exponentially with force whereas the porosity drops off linearly over the same force range [29]. ....	34
Figure 16. Improved compression-test design. ....	40
Figure 17. In a traditional fuel cell design, the compressive force that is necessary for sealing the cell is distributed over both the gasket and the electrode area; however, only the electrode stress affects the electrochemical performance of the cell. ....	41

Figure 18. In the new setup, the sealing and current collection functions are decoupled. The Adjustable Current Collector (ACC) contacts the electrode and is free to translate vertically. The top plate only contacts the gasket; the stress that is applied to the electrode (shown in purple) is therefore completely decoupled from the stress required to seal the cell (shown in red). An o-ring located between the ACC and top plate provides a seal that is independent of ACC position.....	42
Figure 19. (a) The Adjustable Current Collector (ACC) performs the functions of gas distribution to the electrodes, current collection, and transmission of an externally-applied force to the electrode area inside the fuel cell. On the bottom face (b), the serpentine flow field directs the flow of hydrogen or oxygen over the electrode. ....	43
Figure 20. Internal flow paths for hydrogen and oxygen; gas separation is maintained by the presence of the polymer membrane (yellow) and gaskets (blue). ....	43
Figure 21. By turning the leadscrew that is supported by the outer frame, the spring displacement is controlled and compressive force is applied to the ACC. The applied force is transmitted as compressive stress to the electrode area directly below the ACC. ....	44
Figure 22. Pictures of the completed test setup: (a) The fuel cell supported in the outer case and under compressive load; (b) the functional fuel cell unit assembly; and (c) fuel cell disassembled to show the bottom plate (front) and the ACC/top plate assembly (back).....	44
Figure 23. Typical electrochemical impedance response for a PEM fuel cell. At high frequency, the real-axis intercept represents the total ohmic resistance of the cell. The sizes of the semi-circles scale with anode and cathode kinetic losses and the low-frequency tail indicates mass transport limitations [41]. ....	54
Figure 24. The shape of the impedance-response curve depends on the operating cell voltage (overpotential). (a) At high voltage (low overpotential), the response is dominated by sluggish kinetics as evidenced by the relatively large diameter of the semi-circle. (b) At intermediate voltage and overpotential, the reaction kinetics are improved and the semi-circle is smaller. (c) At low voltage (high overpotential), the electrode kinetics are still faster and a low-frequency “tail” feature indicates mass transport limitations [41]. ....	55
Figure 25. V-I curves as a function of applied stress for a cell operating at room temperature (23°C) and 0 psi gas backpressure. Flow rates; 90 cc/min anode, 75 cc/min cathode. 100% relative humidity of inlet gases. ....	58
Figure 26. Performance characterization as a function of applied stress for a cell operating at room temperature (23°C) and 0 psi gas backpressure. (a) Power density curves for 0.8-4.4 MPa. (b) Peak power density as obtained from (a) as a function of applied stress. Flow rates; 90 cc/min anode, 75 cc/min cathode. 100% relative humidity of inlet gases. ....	58
Figure 27. Power density as a function of voltage and applied stress for a cell operating at room temperature (23°C) and no inlet gas backpressure. Flow	

rates; 90 cc/min anode, 75 cc/min cathode. 100% relative humidity of inlet gases.....	60
Figure 28. Effect of backpressure on (a) voltage-current and (b) the power-current curves at 1.6 MPa for a cell operating at room temperature (23°C). Flow rates; 90 cc/min anode, 75 cc/min cathode. 100% relative humidity of inlet gases.....	61
Figure 29. Effect of backpressure on (a) voltage-current and (b) the power-current curves at 4.0 MPa for a cell operating at room temperature (23°C). Flow rates; 90 cc/min anode, 75 cc/min cathode. 100% relative humidity of inlet gases.....	62
Figure 30. Effect of backpressure on the peak power density as a function of applied electrode stress.....	63
Figure 31. Power density as a function of voltage and applied stress for a cell operating at room temperature (23°C) and 10 psi gas backpressure. Flow rates; 90 cc/min anode, 75 cc/min cathode. 100% relative humidity of inlet gases.....	64
Figure 32. Effect of cell temperature on (a) voltage-current and (b) the power-current curves at 1.6 MPa applied stress for a cell operating at 0 psi backpressure. Flow rates; 90 cc/min anode, 75 cc/min cathode. 100% relative humidity of inlet gases.....	65
Figure 33. Effect of cell temperature on (a) voltage-current and (b) the power-current curves at 4.0 MPa applied stress for a cell operating at 0 psi backpressure. Flow rates; 90 cc/min anode, 75 cc/min cathode. 100% relative humidity of inlet gases.....	66
Figure 34. Effect of cell temperature on the peak power density as a function of applied electrode stress. ....	67
Figure 35. Power density as a function of voltage and applied stress for a cell operating at 45°C and 0 psi gas backpressure. Flow rates; 90 cc/min anode, 75 cc/min cathode. 100% relative humidity of inlet gases. ....	68
Figure 36. Cell ohmic resistance as a function of applied stress for a cell operating at room temperature (23°C) and different inlet gas backpressures. The ohmic resistance was obtained by fitting a line to the linear region of each V-I corresponding curve of the form shown in Figure 25.....	69
Figure 37. Peak power density as a function of backpressure and applied stress.....	70
Figure 38. Peak power density as a function of cell temperature and applied stress.....	70
Figure 39. Impedance response for a cell operating at 65°C and 0 psi backpressure under 1.6 MPa applied electrode stress. The high-frequency real-axis intercept (at small $Z'$ ) corresponds to the cell ohmic resistance, and the size of the semi-circle reflects the extent of kinetic losses at the electrodes. ....	71
Figure 40. Effect of increasing applied electrode stress from 1.6 MPa to 4.0 MPa for a cell operating at 65°C and no backpressure. The ohmic resistance (high-frequency intercept) decreases from 0.30Ω to 0.25 Ω and the semi-circle diameter decreases. ....	73
Figure 41. Effect of changing the cell voltage (overpotential) on the impedance response at 1.6 MPa.....	74

Figure 42. Effect of changing the cell voltage (overpotential) on the impedance response at 4.0 MPa. ....	74
Figure 43. Effect of cell temperature on (a) V-I and (b) P-I curves at 1.6 MPa applied stress. Increasing from 23°C to 45°C improves the performance, however, further increasing the temperature to 65°C causes a decline in performance. The large activation losses for the 65°C curve suggest that water may have collected in the cell and blocked the catalyst sites, effectively decreasing the catalyst surface area. ....	88
Figure 44. Peak power density as a function of cell temperature and applied electrode stress. ....	90
Figure 45. 3-D representation of the peak power dependency on cell temperature and applied stress. ....	90

# 1.0 Introduction

## 1.1 The Energy Challenge: The Fuel Cell in Historical Context

The search for alternative, more environmentally-friendly sources of energy will be one of the most daunting projects of the twenty-first century. It will also be a defining moment in the history of technology. As the link between human lifestyle choices and global warming becomes ever clearer, we begin to see that an effective end to the global climate crisis requires a solution that is not only swift but that also can be implemented on a large scale in an economically viable way. Moreover, the solution will be multi-faceted and must address the needs and desires of many different cultures and lifestyles. In this light, technological and consumer-based solutions to the energy challenge are desirable because they empower individuals to make a positive impact on the planet through personal choice.

A promising energy technology that has received widespread attention to date is the fuel cell, an electrochemical system that converts chemical potential energy to useful electrical work. The first fuel cell was built in 1843 by Welsh scientist Sir William Robert Grove [1], but the technology did not undergo significant development until the 1950s, when General Electric launched the nation's first fuel cell research program. The fuel cell gained considerable attention for its use as a power system aboard the spacecraft used during Project Gemini, NASA's human space flight program in 1965-1966 [2]. In the subsequent decades, fuel cells have been explored for a variety of applications including stationary power generation systems, consumer electronics, and, perhaps most popularly, as an alternative to the traditional Internal Combustion Engine (ICE) in automobiles.

A fuel cell can take many different forms that are distinguished by, among other factors, the operating temperature of the cell, the materials used and the types of fuel and oxidant consumed for power generation. One type in particular, the Proton Exchange Membrane<sup>1</sup> (PEM) fuel cell, has received a large fraction of the research and commercial

---

<sup>1</sup> In the literature, PEM is alternatively defined as Polymer Electrolyte Membrane.

attention to date. PEM fuel cells are typically used for intermediate-scale power generation on the order of 1-10 W for consumer electronics and 100s of kW for transportation [3]. The operating temperature, typically 80°C, is low in comparison with other fuel cells<sup>2</sup> which significantly simplifies the system and broadens its range of applications. PEM fuel cells utilize hydrogen gas as the fuel and pure oxygen or air as the oxidant.

PEM fuel cells prove advantageous over traditional fossil-fueled power generation for a number of reasons that are inherent to the way energy is converted in the cell. Firstly, the chemical reaction to produce electrical power from hydrogen and oxygen gas is direct (no combustion is required) and theoretically has no environmentally harmful byproducts (the only byproduct is liquid water). Secondly, the energy conversion process can be more efficient than for an ICE, with fuel cell theoretical efficiencies upwards of 80%. Fuel cell units are modular and can be assembled into stacks of many sizes in order to meet a variety of power needs. Finally, fuel cells have no moving parts and this enhances their durability and minimizes the amount of maintenance required [3].

A good testament to the perceived promise of the PEM fuel cell is the announced implementation of fuel cells (both as stand-alone systems, and in fuel cell-battery hybrid form) in next-generation automobiles from some of the world's top auto makers [4]. Some of the better-known fuel cell cars that are currently under development include the Honda *FCX*, the GM *HydroGen3* and *Equinox*, and the Ford *Focus FCV*. Although these vehicles are quite expensive to manufacture and run, test fleets have been released in selected major cities in the United States and a number of auto makers, including Honda and BMW, have announced plans to release their first publicly available fuel cell vehicles within the next couple of years. Honda has also developed a home refueling unit that reforms natural gas on-site to generate hydrogen. The application of fuel cells as alternative power systems for transportation extends beyond automobiles; recently, Boeing's Phantom Works division successfully tested its first hydrogen fuel cell plane [5].

---

<sup>2</sup> Solid Oxide Fuel Cells, for instance, operate in the range of 500-1000 °C [3].



A common and valid criticism of the PEM fuel cell in its current implementation is that it does not yield a closed-cycle, entirely “green” power conversion process. This is because of the requirement for pure hydrogen gas, which is typically supplied commercially from reformed fossil fuels. This aspect of fuel cells has caused quite a stir, both in academia and in the media, and there is much debate about whether the so-called “Hydrogen Economy” that will support fuel cells could ever come to fruition in an economically viable way [6, 7]. However, if we are to imagine for a moment that this upstream hydrogen-supply problem can be solved – and there are many scientists who argue that it can [8, 9] – then the benefit of the fuel cell becomes clear and the motivation behind its development becomes even stronger.

## **1.2 Fuel Cells: State of the Art**

In order to appreciate the fuel cell’s capability for power generation, we compare its performance to that of batteries which serve as a convenient technological benchmark. Fuel cells are similar to batteries in that both are electrochemical systems that convert chemical bond enthalpy into useful electrical work via separate anode and cathode reactions. While a battery’s power capability varies with the state of charge, the fuel cell is capable of sustaining performance, at least in the short term, as long as fuel and oxidant are supplied. Since a fuel cell is an open system rather than a closed system like the battery, fuel cell systems often require additional components to set and maintain desirable operating conditions such as cell temperature, gas flow rate and relative humidity of inlet gases.

The PEM fuel cell has an energy density that is comparable to that of an ICE, and up to an order of magnitude higher than traditional battery technologies (Figure 1). This can be interpreted to mean that for a given power requirement, the effective lifetime per kilogram of a fuel cell is longer than that for a battery. This fact motivates the use of fuel cells for long-term power needs for which battery lifetime is insufficient. However, even the best-performing PEM fuel cells have a power density per kilogram that is lower than that of most batteries and ICEs, meaning that the size and weight requirement of a fuel cell that is needed to achieve a certain power output is higher than that of competing

technologies. This requirement has proven to be one of the main challenges to large-scale implementation of fuel cells in automobiles.

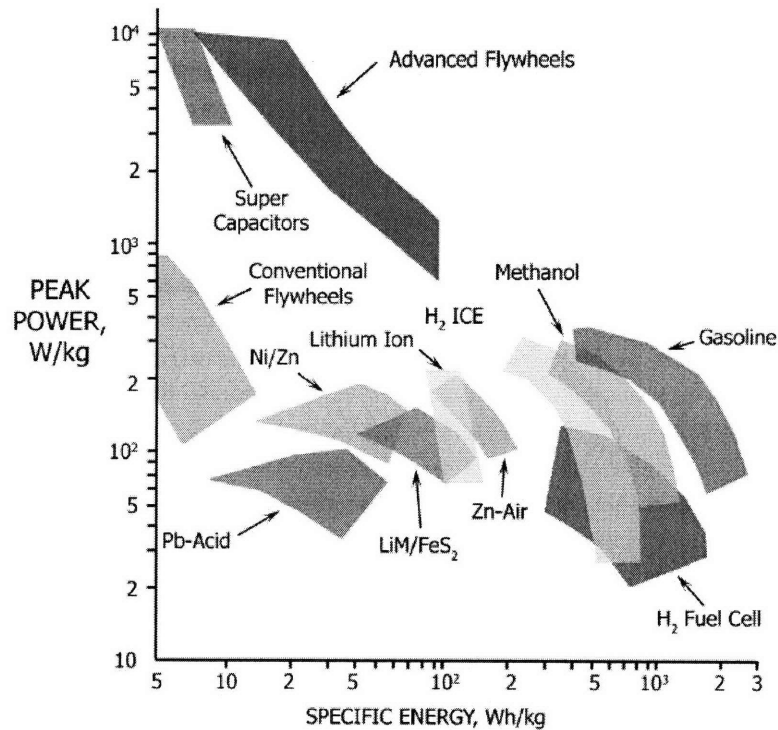


Figure 1. Ragone plot of energy and power density comparisons between different energy conversion and storage technologies.

### 1.3 Challenges for Large-Scale Implementation

Although PEM fuel cells hold promise as power supply alternatives, a number of factors challenge their large-scale implementation at the consumer level. Firstly, the historically high cost of fuel cells has been prohibitive. This cost is largely attributed to the use of platinum as a catalyst, as well as the current lack of efficient large-scale manufacturing processes for making fuel cell components [10]. Much work has been done to reduce the amount of platinum that is needed in a fuel cell; today, a platinum loading of 0.2 mg Pt/cm<sup>2</sup> is typical, whereas platinum loading was once as high as 28 mg Pt/cm<sup>2</sup> [3] in early systems. As a result, the fuel cell cost has dropped significantly; Ballard Power Systems, a leading fuel cell manufacturer, achieved a cost of \$73/kW in 2005 for a predicted

volume production of 500,000 fuel cell stack units per year [9]. The Department of Energy has set fuel cell cost targets at achieving \$45/kW by 2010 and \$30/kW by 2015 [11] and this is thought to be an upper ceiling that much be broken in order for fuel cells to be economically viable on a large scale.

Secondly, fuel cells are subjected to a wide range of operating conditions throughout their functional lifetime, and these varying conditions can cause cyclic mechanical stresses and, ultimately, degradation of fuel cell performance. In addition to mechanical degradation, the fuel cell catalyst experiences a 'poisoning' effect over time which effectively reduces the surface area that is available for chemical reactions. These factors limit the operational lifetime of the cell to about 2000 hours on average today [12]; in order to be a competitive technology, targets have set the necessary operational lifetime at 5000 hours or higher for transportation applications [13].

The maximum voltage of a single PEM fuel cell is thermodynamically limited to roughly 1.2 V (the origin of this voltage is discussed further in section 2.1.3). This voltage is far from sufficient for large power requirements, such as in an automobile. Therefore, to accommodate practical voltage and power needs, fuel cells are typically stacked in series. These stacks can be quite large and it can be challenging to integrate them into current vehicles. Additionally, as discussed earlier, many fuel cell systems require complex control and supply systems such as external pumps, inlet gas humidifiers, mass flow controllers, and backpressure regulators, among other components. This only adds to the size and weight of a fuel cell system and makes it ever more challenging to develop efficient fuel cells for commercial use. In the long term, success of this technology will depend on the resolution of this significant engineering challenge.

## **2.0 Background**

### **2.1 Fuel Cell Operating Principles**

#### **2.1.1 PEM Fuel Cell Components**

As in all electrochemical cells, a fuel cell has as its most basic components a set of electrodes and electrolyte by means of which the electrochemical reactions occur. The Proton Exchange Membrane fuel cell is so-called because it uses a thin, proton-conducting polymer membrane as the electrolyte. This material – typically Nafion, which is manufactured by DuPont – is unique for its ability to selectively conduct protons while blocking the flow of electrons. The significance of this becomes clear when the basic fuel cell chemical reactions are examined in Section 2.1.2. In practice, one of the most commonly used membranes is the Nafion No. 117 [14] which is 183 microns in thickness.

The electrodes in a PEM fuel cell take the form of distributed catalyst particles (most commonly platinum) that are supported on a porous carbon paper or carbon cloth. Together, the platinum and carbon support are referred to as the Gas Diffusion Electrode (GDE) or Gas Diffusion Layer (GDL). An inherent and necessary property of these GDEs is their porosity, which enables the reactant gases to penetrate the electrode structure and access the catalyst. This three-dimensional structure (Figure 2) thereby effectively increases the electrode surface area. Other functions of the GDE include helping with water management and conducting ions into or away from the triple phase boundary of gas, electrolyte and catalyst once ions are formed [15]. In a typical system, the in-plane dimension of the GDE can vary from 5 cm<sup>2</sup> to 50 cm<sup>2</sup> or larger.

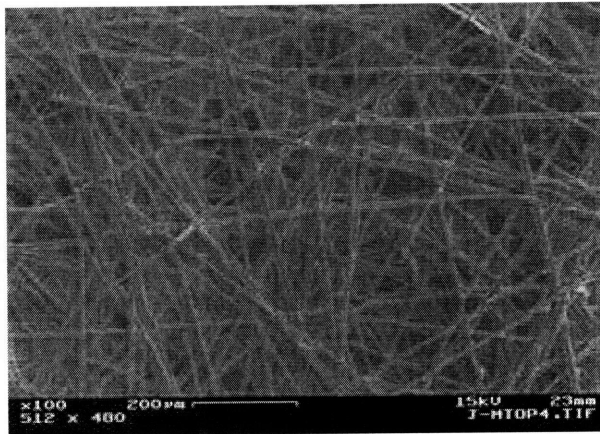


**Figure 2.** The porous structure of the gas diffusion electrode (GDE) on the micro-scale allows hydrogen and oxygen to access the electrode catalyst sites [16].

The GDEs are hot-pressed onto either side of the Nafion membrane to create a Membrane Electrode Assembly, or MEA (Figure 3). The MEA is the basic functional unit of the fuel cell and can be purchased commercially or manufactured in-house. During fuel cell operation, the MEA is constrained between two stiff outer plates that hold the cell together and provide mechanical stability and protection, among other functions.

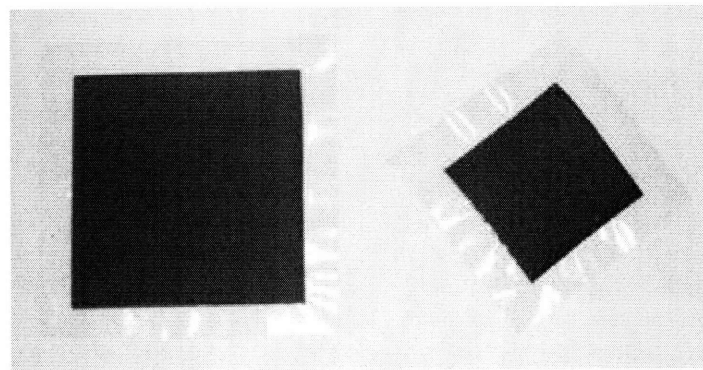


**Figure 3.** Membrane Electrode Assembly (MEA) for a PEM fuel cell [17]. The electrolyte is a thin translucent polymer and the electrodes/gas diffusion backings appear in black.

In order to draw current from the cell, it is necessary that the reaction sites in the GDEs be in contact with an electrically conductive medium, typically referred to as a *current collector*. For good cell performance, current collectors must have low electrical resistance and good thermal conductivity in order to facilitate heat management in the

fuel cell. To meet these needs, current collectors are often made from graphite, although more recent investigations have explored the use of metal current collectors [18, 19] as a cheaper and simpler alternative. The current collectors are often mechanically integrated into the outer plate structure.

Inlet gases are distributed over the electrode areas by a flow path that is machined into the surface of the current collector. The flow path consists of a channel or series of channels which serve to constrain the gases to the electrode area and often takes the form of a simple serpentine flow path, as shown in Figure 4. The portion of the current collector that lies between the flow channels and contacts the electrode is referred to as the *rib*, and the design of a good fuel cell requires careful optimization of the flow channel and rib surface area ratio. In addition to gas distribution, the flow field plays an important function in helping to remove the product water from the cell.

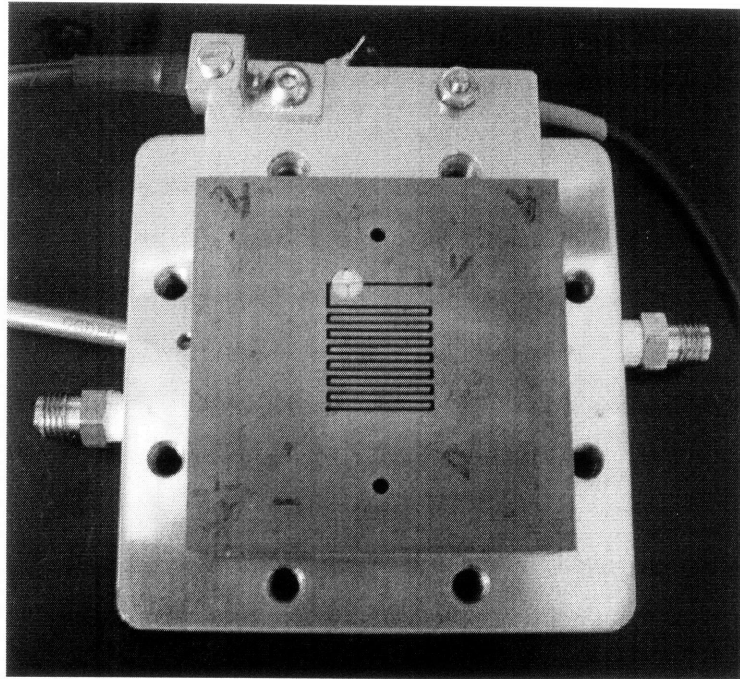


**Figure 4. Graphite current collector with machined serpentine flow field in a traditional PEM fuel cell setup.**

It is essential that the fuel cell reactant gases are constrained to the fuel cell electrode area and are prevented from escaping into the environment where they could pose a safety hazard. In addition to being unsafe, the fuel cell will not perform well without a good seal. To address this, gaskets are inserted into the fuel cell during

assembly. When the outer plates are bolted together, the gaskets are compressed and an adequate seal is achieved.

Figure 5 shows a fully-assembled single cell that is ready for use. As has been mentioned, fully operational fuel cell system may require additional components beyond the unit fuel cell, such as mass flow controllers to regulate the inlet gases, a humidifying system for the inlet gases, pumps, temperature control (both heating and cooling), a backpressure regulation system, and a controller and data acquisition system. Fuel cells that are integrated into larger power generation systems may also require Balance of Plant components such as heat exchangers or additional pumps.

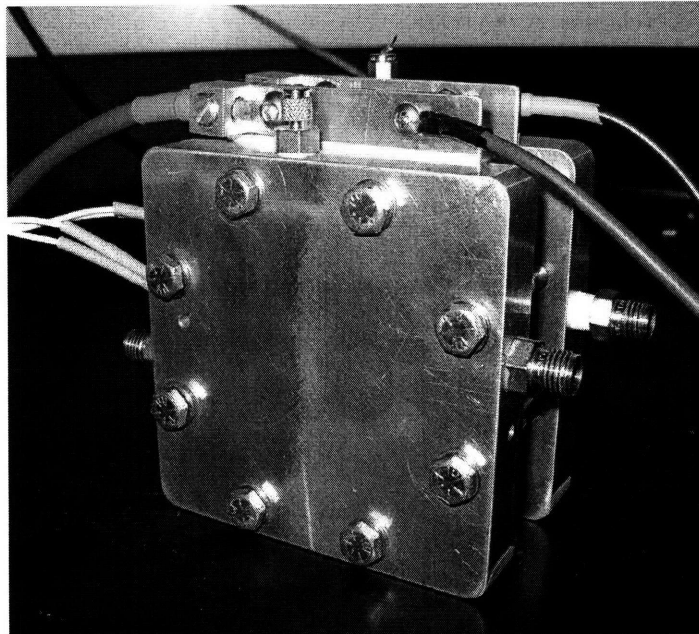


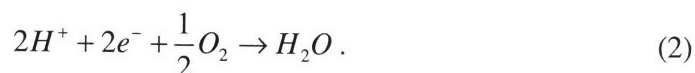
**Figure 5. Fully assembled PEM fuel cell.**

### **2.1.2 PEM Fuel Cell Chemical Reactions**

In a PEM fuel cell, hydrogen gas is supplied to the anode side and oxygen gas or air is supplied to the cathode side. Chemical energy is converted to electrical work via two half cell reactions that together form a redox pair. On the anode side, hydrogen is oxidized into protons and electrons by



The protons are conducted directly through the membrane; the electrons, which are barred from flowing through the membrane, flow through an external load where they perform useful electrical work. The protons and electrons then recombine and reduce oxygen on the cathode side to form water, by the reaction



The overall fuel cell reaction is thus



with water as the only byproduct. A summary of the cell reactions is depicted in Figure 6.

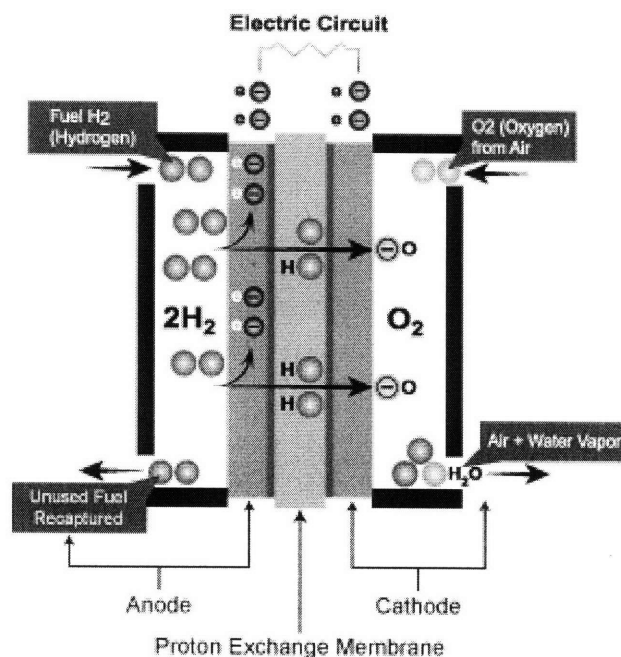


**Figure 6. Summary of cell reactions in a PEM fuel cell. At the anode, hydrogen is oxidized into protons, which travel through the membrane, and electrons, which are forced around an external circuit. At the cathode, oxygen, protons and electrons combine to produce water [20].**



### 2.1.3 Open Circuit Voltage (OCV)

Each half-cell reaction occurs at a unique electrode potential that depends on the chemical species involved as well as the conditions at the electrode. The standard electrode potential  $\mathcal{E}^o$  for a variety of half-cell reactions at standard conditions<sup>3</sup> is easily obtained from a reference table [21]. For a PEM fuel cell, the standard reduction half-cell potentials are

$$\begin{aligned}\mathcal{E}^o_{anode} &= \mathcal{E}^o_{H^+/H} = 0V \\ \mathcal{E}^o_{cathode} &= \mathcal{E}^o_{O_2/O} = 1.229V\end{aligned}$$

The net reversible cell voltage is then

$$\mathcal{E}^o_{cell} = -\mathcal{E}^o_{anode} + \mathcal{E}^o_{cathode} = 0V + 1.229V = 1.229V \quad (4)$$

at standard conditions. For a PEM fuel cell operating at non-standard conditions, the reversible cell voltage is given by

$$\mathcal{E}_{cell} = \mathcal{E}^o_{cell} - \frac{RT}{zF} \ln \frac{\prod a_i^{v_i}_{products}}{\prod a_i^{v_i}_{reactants}} \quad (5)$$

where T is the temperature, R is the universal gas constant,  $v_i$  is the stoichiometric coefficient associated with each species in (3),  $a_{products}$  is the activity of the product species,  $a_{reactants}$  is the activity of the reactant species, z is the number of electrons involved in the cell reaction (here,  $z = 2$ ) and F is the Faraday constant. The activity for an idea gas,  $a_i$ , is given by  $a_i = \frac{\rho_i}{P^o}$ , where  $\rho_i$  is the partial pressure of the gas and  $P^o$  is atmospheric pressure. The partial pressure can further written as  $\rho_i = x_i P_i$  where  $x_i$  is the molar concentration of species  $i$  and  $P_i$  is the gas pressure. Substitution of this form into (5) yields the cell potential dependency on inlet gas pressure:

---

<sup>3</sup> Standard conditions refers to 25 °C and 1 atm.

$$\mathcal{E}_{cell} = \mathcal{E}^{\circ}_{cell} - \frac{RT}{zF} \ln \frac{\prod \left( \frac{x_i P_i}{P^{\circ}} \right)^{v_i}_{products}}{\prod \left( \frac{x_i P_i}{P^{\circ}} \right)^{v_i}_{reactants}}. \quad (6)$$

For a PEM fuel cell with a net reaction according to (3), (6) becomes

$$\mathcal{E}_{cell} = \mathcal{E}^{\circ}_{cell} - \frac{RT}{2F} \ln \frac{\left( \frac{x_{H_2O} P_{H_2O}}{P^{\circ}} \right)}{\left( \frac{x_{H_2} P_{H_2}}{P^{\circ}} \right) \left( \frac{x_{O_2} P_{O_2}}{P^{\circ}} \right)^{\frac{1}{2}}}. \quad (7)$$

(5) is known as the Nernst equation and is one of the most important tools in electrochemistry for understanding the thermodynamics of a cell. This voltage is predicted solely by the thermodynamics of the electrode reactions and does not account for any losses in the cell that result from current generation. Therefore, this voltage is only achieved practically when no current is being drawn in the cell (hence the name “Open Circuit Voltage”). To describe the complete voltage-current behavior of a fuel cell, we must consider other mechanisms that affect how quickly and effectively the chemical reactions proceed as well as how chemical species are transported in the cell.

The OCV of a cell can also be calculated directly from knowledge of the Gibbs Free Energy change,  $\Delta G_r^{\circ}$ , between the reactant species and product species in (3) by

$$\mathcal{E}^{\circ} = -\frac{\Delta G_r^{\circ}}{zF}. \quad (8)$$

$\Delta G_r^{\circ}$  is given by

$$\Delta G_r^{\circ} = \Sigma (v_p \mu_p^{\circ}) - \Sigma (v_r \mu_r^{\circ}) \quad (9)$$

where  $\mu$  is the chemical potential associated with each product or reactant in (3). The chemical potentials are known quantities and are easily obtained from a thermodynamic reference table [22]. The Gibbs Free Energy change is related to the change in enthalpy,  $\Delta H_r^\circ$ , and the change in entropy,  $\Delta S_r^\circ$  between the reactant and product state by

$$\Delta G_r^\circ = \Delta H_r^\circ - T\Delta S_r^\circ. \quad (10)$$

Combining (8) with (10) and taking the derivative with respect to temperature yields

$$\frac{d\varepsilon^\circ}{dT} = \frac{\Delta S_r^\circ}{zF}. \quad (11)$$

Typically,  $\Delta H_r^\circ$  and  $\Delta S_r^\circ$  are both negative for the reaction (3), and therefore the reversible potential  $\varepsilon^\circ$  tends to decrease with increasing cell temperature by (11). The implications of this for cell performance will be discussed in greater detail in following sections.

#### 2.1.4 Typical Voltage-Current (V-I) Curve

Figure 7 depicts a typical voltage-current (V-I) curve for a PEM fuel cell. As expected, the voltage at zero current is close to the OCV predicted by the thermodynamics. Ideally, a fuel cell would maintain this reversible potential regardless of how much current is drawn from the cell. In reality, however, there are certain losses, referred to as *overpotentials*, associated with the electrode reactions that cause the cell voltage to decrease with increasing current. The overpotential  $\eta$  is attributed mainly to three sources: activation losses,  $\eta_{act}$ ; ohmic resistance,  $\eta_\Omega$ ; and mass transport limitations  $\eta_t$ . The different overpotential components dominate the cell performance in specific regions of the V-I curve as shown in Figure 8.

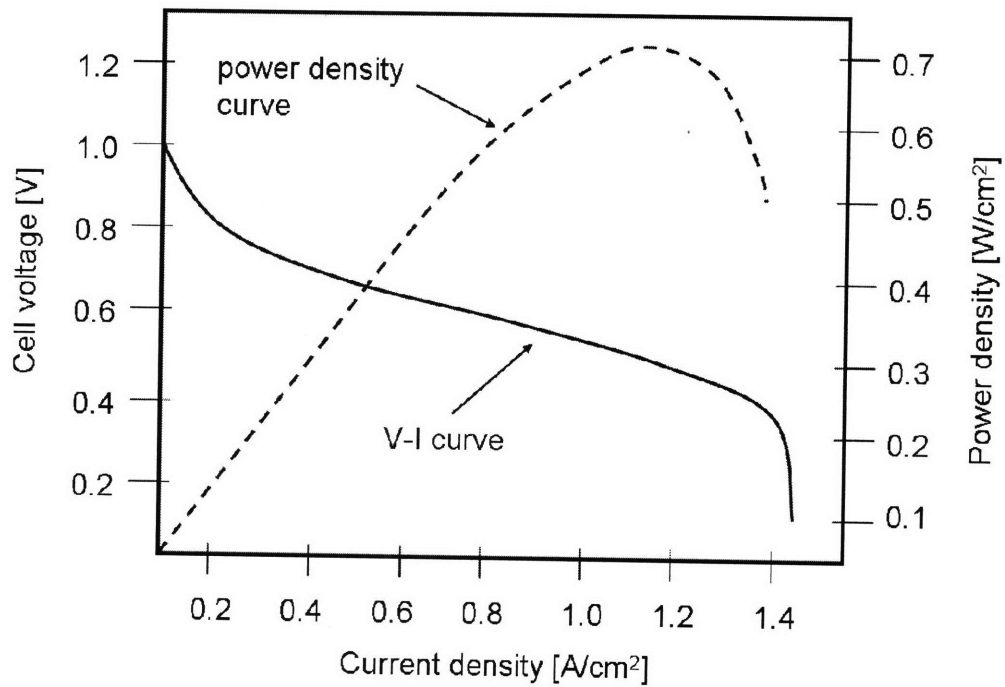


Figure 7. Typical voltage-current (V-I) and power-current (P-I) curves for a PEM fuel cell. The P-I curve is obtained from the product of voltage and current at each point along the V-I curve.

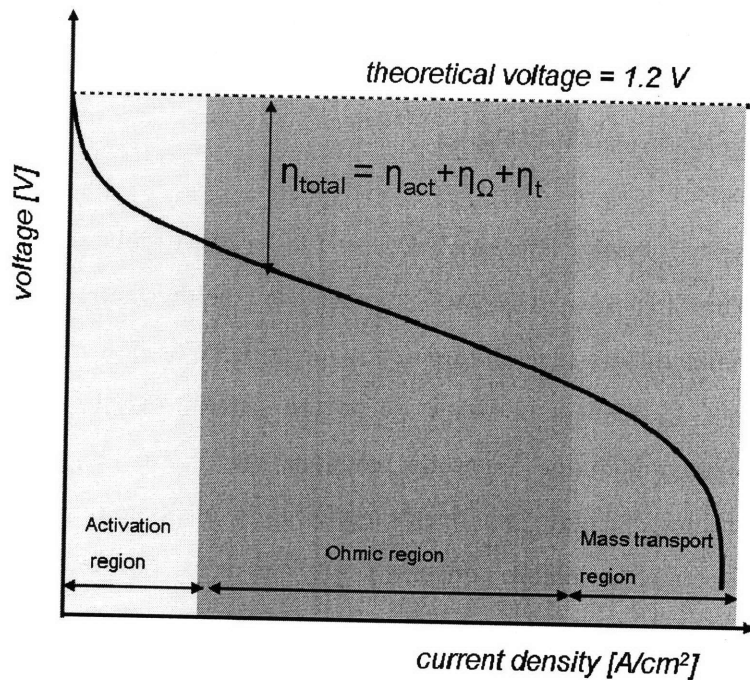


Figure 8. Contributions to the net voltage loss (overpotential) in a PEM fuel cell: activation, ohmic, and mass transport overpotentials.

### *Activation Losses*

Fuel cell performance in the high-voltage, low-current regime, as depicted in Figure 8, is dominated by activation (kinetic) losses. These losses occur because a certain amount of chemical energy is required to “activate” or overcome sluggish electrode kinetics and generate current. This activation energy comes directly from the chemical potential energy stored in the fuel and decreases the net energy available for electrical work. This process manifests experimentally as a decrease in voltage with increasing current generation at voltages close to OCV, and in certain cells can be quite significant over the entire voltage range.

### *Ohmic Losses*

The electrical resistance of the cell typically has a significant effect on the shape of the V-I curve, particularly in the mid-voltage operating range. This net resistance is attributed to a number of different sources, including the bulk resistance of the current collector materials and membrane, interfacial contact resistance (ICR) between different layers of the cell, and resistance of the electrical leads.

### *Mass Transport Losses*

The water that is produced as a byproduct of the cell cathode reaction must be removed quickly to avoid flooding the cell. If too much water remains in the cathode side, it can block the GDE pores and restrict the ability of oxygen to access the catalyst sites. At low current (low water generation rate), this is typically not difficult to achieve. However, as the current generation increases it is challenging to remove water faster than it is being produced. As a result, cell voltage often drops off rapidly at high current densities.

## **2.1.5 Power**

The tradeoff between voltage and current in a PEM fuel cell leads to the typical power-current curve depicted in Figure 7. The peak power of a PEM fuel cell occurs in the high-current, low-voltage regime and typically falls in the range of 0.5-1 W/cm<sup>2</sup>. In order to supply a high voltage and power density on the order of what is required for

transportation, the fuel cells must be stacked in series. The number of cells required for these applications is high and the resulting fuel cell stacks can be quite large and heavy. It is no easy task to design an efficient fuel cell stack, and the academic attention paid to increasing fuel cell power density is so high largely for this reason.

### **2.1.6 Fuel Cell Design: Parameters that Affect Power Output**

The independent parameters that affect the fuel cell performance can be broken up into two genres: *engineering parameters* and *operating parameters*. The former refer to the material and dimensional design decisions that an engineer makes when designing a fuel cell system. The latter describe the parameters that are fixed at the time of fuel cell operation, such as cell temperature or fuel flow rate. It is important to consider both sets of parameters when optimizing fuel cell performance, and furthermore, to consider how the two sets of parameters can influence one another in the fuel cell operational environment.

A summary of the important engineering and operating parameters for a PEM fuel cell is presented in Table 1. The first column lists performance metrics which directly affect the power output of the cell, as described in the previous section. The ohmic resistance is attributed to several sources, including the bulk electrical resistance of the current collectors, the protonic resistance of the membrane, and the interfacial resistance between conducting layers. It is noted that many engineering and operating parameters appear multiple times in the table, and that changing one parameter can have a significant and unexpected effect on all aspects of the fuel cell performance. This inherent coupling between parameters is a significant challenge for the fuel cell design engineer and will be discussed further in following sections.

Performance metric		Engineering parameter	Operating Parameters
Ohmic resistance	Bulk electrical resistance	Current collector material Current collector thickness Electrical leads (type, length)	Cell temp.
	Interfacial Contact Resistance	Current collector material Current collector surface contact area	Clamping stress
	Protonic resistance	Membrane material Membrane thickness	Cell temp. Humidity temp. Clamping stress
Mass transport/water management		Flow-field channel dimensions (width and length)	Cell temp. Humidity temp. Backpressure H <sub>2</sub> /O <sub>2</sub> stoichiometry Clamping stress

**Table 1. Engineering and operating parameters of PEM fuel cells that affect performance.**

### 2.1.7 Expected Results of Variations in Selected Operating Parameters

#### *Cell Temperature*

By considering Equation 11, it is clear that the reversible cell voltage decreases with an increase in operating temperature since  $\Delta S_r$  is negative for the net PEM fuel cell reaction. However, operating at higher temperatures can lower the kinetic losses that occur at the electrodes during current generation. Additionally, the protonic conductivity of Nafion is enhanced at higher operating conditions [23, 24], leading to a reduction in net cell ohmic losses. In general, then, it is expected that cell performance will improve as the operating temperature increases.

#### *Relative Humidity of Inlet Gases*

The humidification of inlet gases can play a major role in affecting the fuel cell performance. Normally, humidification is achieved by flowing the gases through heated water bottles, where they absorb moisture until saturation is reached in the gas phase. The

cell temperature may or may not be the same as the bottle temperature; if the cell temperature is higher, the gas temperature increases while in the cell and the relative humidity of the gas decreases. If instead the cell temperature is lower, then water will condense out of the gas as it flows through the cell.

Inlet gases that are humidified at less than 100% relative humidity with respect to the cell temperature create a drying environment for a fully hydrated cell membrane [25]. Since hydration is essential for good proton conductivity, gases that are too dry will cause the ohmic resistance of the cell to increase over time as drying occurs. If the gases carry too much moisture, however, the liquid condensation can cause flooding, and mass transport limitations at high current densities will worsen. The effect of cell drying is less severe at lower cell temperatures; however, for cells operating above 60°C, the high temperature exacerbates the water loss from the membrane. To avoid extreme drying of the cell, gases should always be humidified in this higher temperature range [3].

### *Cell Backpressure*

Pressurization of the inlet gases improves fuel cell performance by increasing the coverage of reactant at the electrode catalyst sites [3]. Higher coverage decreases the activation overvoltage, particularly at the cathode side where activation losses are more severe than for the anode. The result of higher operating pressure is typically a constant net increase in voltage as a function of current density. Additionally, higher inlet gas pressure increases the OCV by (7), which further enhances the cell performance.

## **2.2 PEM Fuel Cell Compression**

It is well known that fuel cell performance varies dramatically based on the magnitude of force used to clamp together the outer plates of the fuel cell assembly [31, 34-38]. In a typical fuel cell setup, this clamping force is varied by increasing or decreasing the torque on the bolts that connect the outer plates. At low clamping magnitudes, an increase in the clamping force improves the fuel cell power density as the inner components of the cell are brought into better electrical contact and the Interfacial Contact Resistance (ICR) between material layers decreases. As clamping force increases, however, the amount of



improvement in performance that is possible levels off. This is generally attributed to the fact that GDE porosity decreases with high clamping force which harms mass transport and water removal capability [26]. Therefore, there exists a clamping force beyond which there is little improvement or even a decrease in cell performance. Overall, the force-dependent performance of a fuel cell reflects the tradeoff between the two competing effects of improved ICR and worsened mass transport. It is useful to quantify how the fuel cell performance changes with clamping force and to identify why these changes occur so that fuel cell design and performance may be optimized.

### **2.2.1 Investigations in the Literature**

Quite a few research groups have studied the effect of mechanical compression on PEM fuel cell performance. Techniques have spanned from analytical to experimental and have focused on the effect of compression on individual components as well as the entire fuel cell system.

#### *Effect of Compression on Interfacial Contact Resistance*

A good physical description of the significance of contact resistance is given by Mishra et al. [27] in which the contact resistance between current collector and gas diffusion layer is explored. The authors attribute contact resistance to surface roughness (Figure 9) on the molecular scale of two contacting materials. Surface roughness prevents the two materials from fully contacting (Figure 10) and causes a voltage drop across the contact interface. As clamping pressure is increased, the roughness features on the surfaces of the two materials are deformed so as to increase the overall surface area that is in good electrical contact. Consequently, the resistance to current flow between the two surfaces decreases.

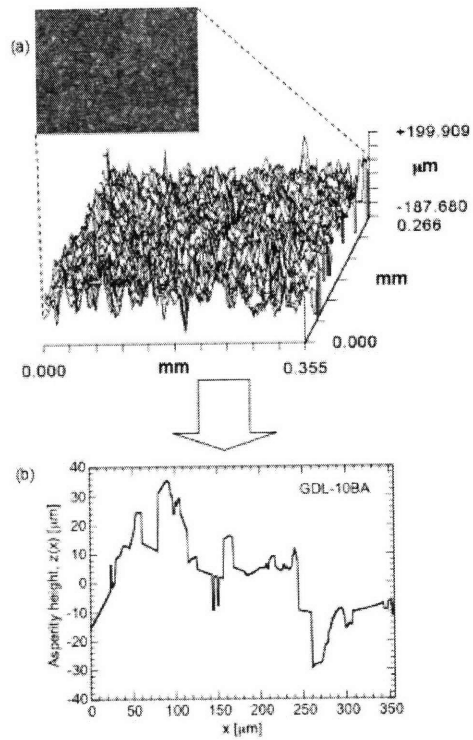


Figure 9. Imaging of surface roughness of a gas diffusion layer in a PEM fuel cell [27].

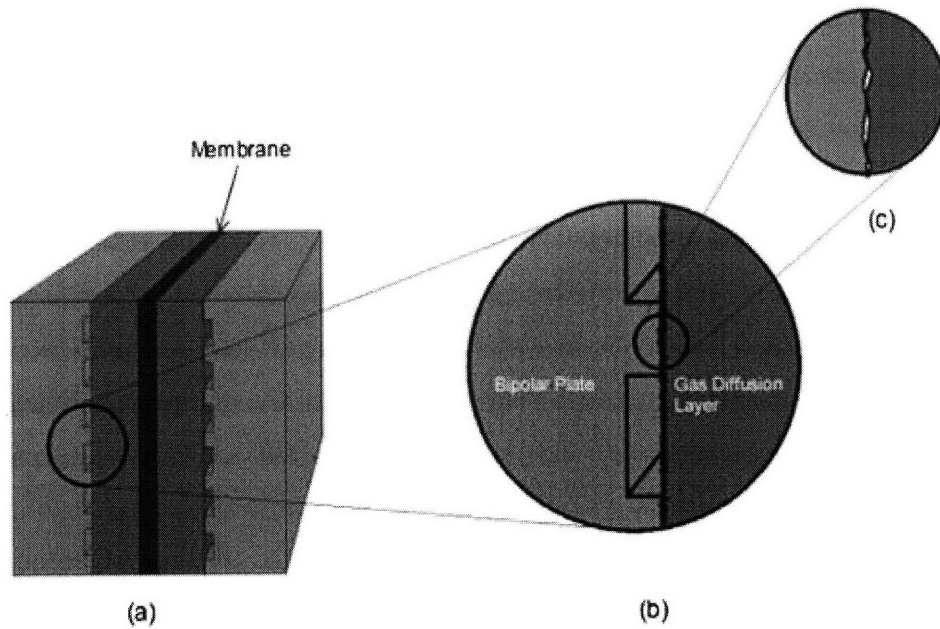
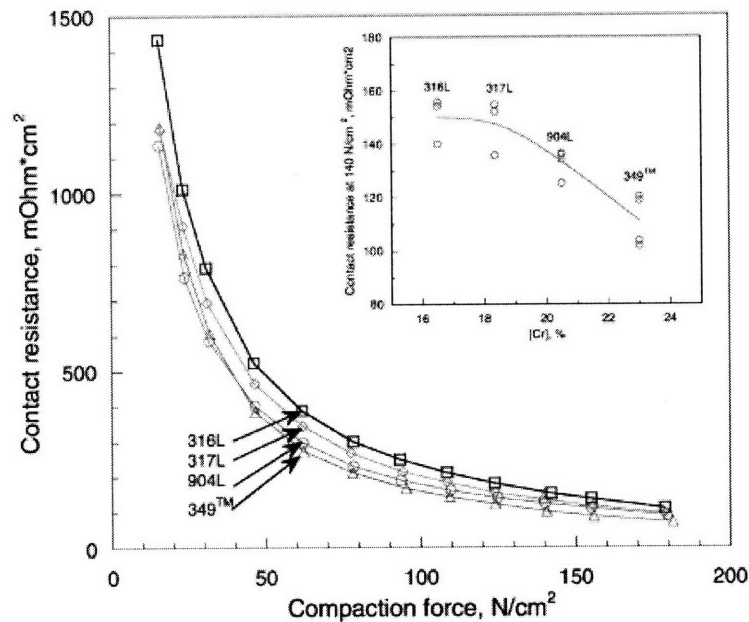


Figure 10. Surface roughness limits the surface area contact between two materials and contributes to the contact resistance across the interface [27].

Since the surface morphology is material-dependent, the contact resistance depends on the material properties of the two contacting layers. Wang et al. [28] measured the effect of compression on the magnitude of ICR for stainless steel grades 316L, 317L, 904L, and 349<sup>TM</sup>. ICR is shown to decrease exponentially with increasing compression for all grades with the largest reductions occurring between 0 and 50 N/cm<sup>2</sup> (Figure 11). 316L is shown to have the largest overall ICR, and 349<sup>TM</sup> the smallest, regardless of compression magnitude. The inset plot shows the relationship between chromium content of the steel grade and contact resistance at 140 N/cm<sup>2</sup>. These data demonstrate that ICR is dependent upon both the material composition and the physical environment, i.e. the contact pressure at the interface with surrounding materials. Other investigations have been performed [19] which confirm this relationship and which quantify the ICR-force relationship for other materials besides steels.



**Figure 11. Comparison of force-dependent contact resistance for stainless steel grades 316L, 317L, 904L and 349<sup>TM</sup>. Contact resistance decreases exponentially with increasing compaction force and is consistently highest for 316L [28].**

In addition to the current collector material, ICR has been shown to be sensitive both to GDL type used and the physical morphology of the flow field in contact with the GDL [29]. Zhou et al. tested how ICR varies with rib spacing (the distance between flow channels) for different GDLs and for different clamping pressures. The results are shown

in Figure 12 and demonstrate the dependence of ICR on features of the current collector/flow distributor design.

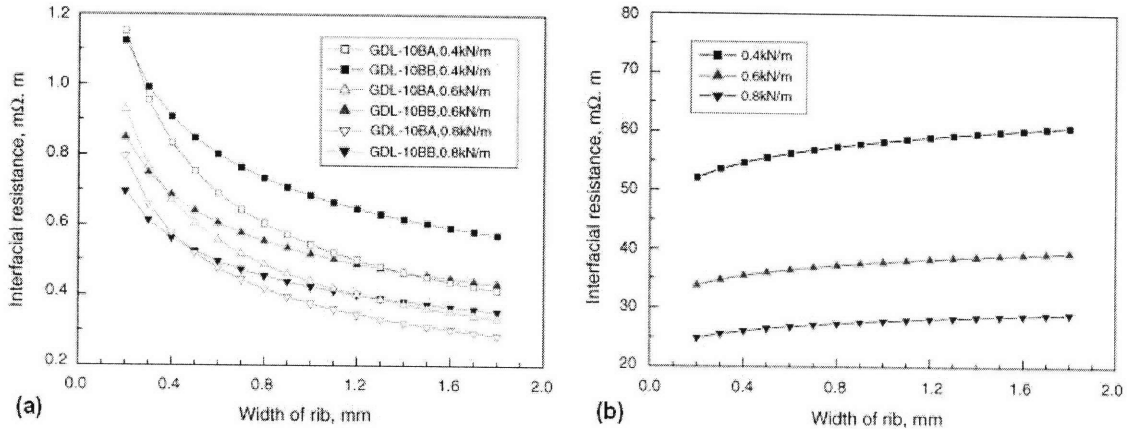


**Figure 12. Dependence of contact resistance on flow-field rib width for different GDL types (a) and compaction force magnitudes (b) [29].**

### *Effect of Compression on Gas Diffusion Layer Structure and Water Management Capability*

A number of works have examined the effect of compression on GDL properties and performance [30-33]. Itonen et al. [32] tested the effect of clamping pressure on porosity, in-plane and through-plane permeability, and thermal impedance of the GDL, among other parameters, for a variety of commercially-available GDLs (both carbon cloth and carbon paper). The general finding was that the sensitivity of a GDL to changes in clamping pressures depends on the type of GDL used, with the carbon cloths showing a significantly more drastic reduction in permeability than the carbon papers at higher clamping pressure.

Zhou et al. [29] studied the decrease in porosity as a result of compression for two different GDLs as a function of current collector rib width. A linear decrease in porosity was observed in all cases. Somewhat counter-intuitively, the wider the rib width, the smaller the porosity decrease over a fixed range of clamping pressures.

Bazylak et al. [30] illuminated an interesting feature that could help GDLs maintain good performance even at high stress and low porosity. In this paper, the authors used Scanning Electron Microscopy (SEM) to image the GDL at the micro-scale

in order to visualize the effect of compression. The GDLs used in this study were coated with PTFE in order to make the GDL more hydrophobic and thereby enhance the capability for water removal. Figure 13 illustrates the pristine, uncompressed sample and Figure 14 shows the change in fiber structure as a result of various compression magnitudes held for five minutes. The changes observed in the SEM images are attributed to cracking and peeling of the PTFE layer which harms the hydrophobicity of the GDL, creating localized preferential pathways for water transport in the high-compression areas.

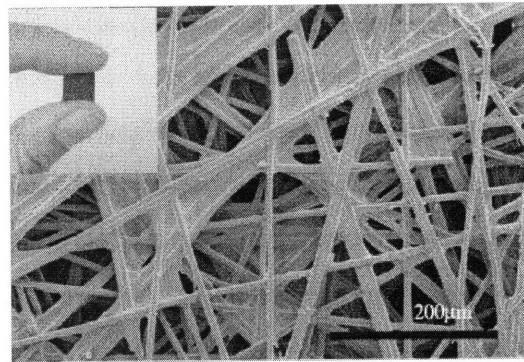


Figure 13. PTFE-coated GDL in pristine form prior to compression [30].

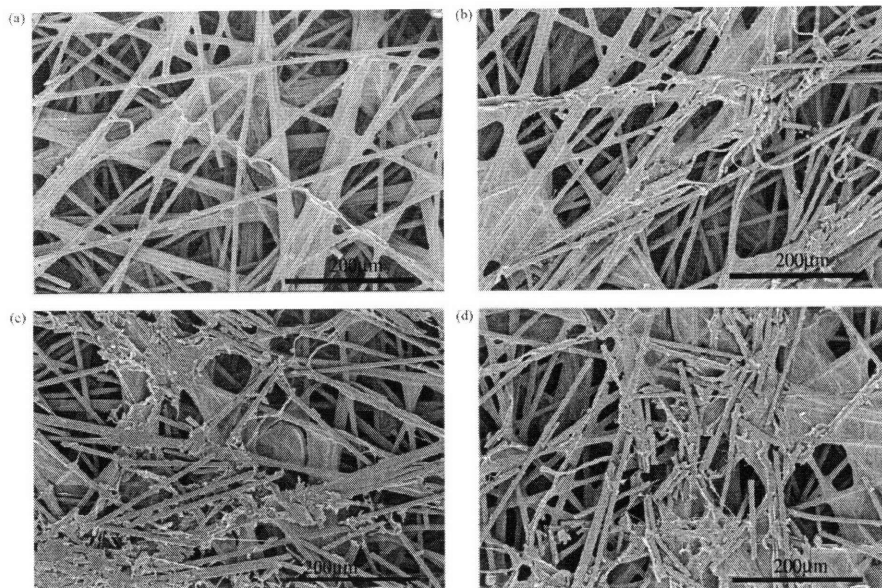


Figure 14. PTFE-coated GDL after being compressed for 5 minutes at (a) 0.18 MPa, (b) 0.36 MPa, (c) 0.68 MPa, and (d) 1.37 MPa. Mechanical degradation of the GDL structure is observed for all cases, particularly for (c) and (d) [30].

A good summary of the relationship of ICR and porosity with applied stress is shown in Figure 15. It is emphasized that while ICR decreases exponentially with increasing stress, porosity decreases linearly over this same range. It is expected that this will lead to some interesting large-scale behavior that will reflect the relative rates of drop-off of these two competing parameters.

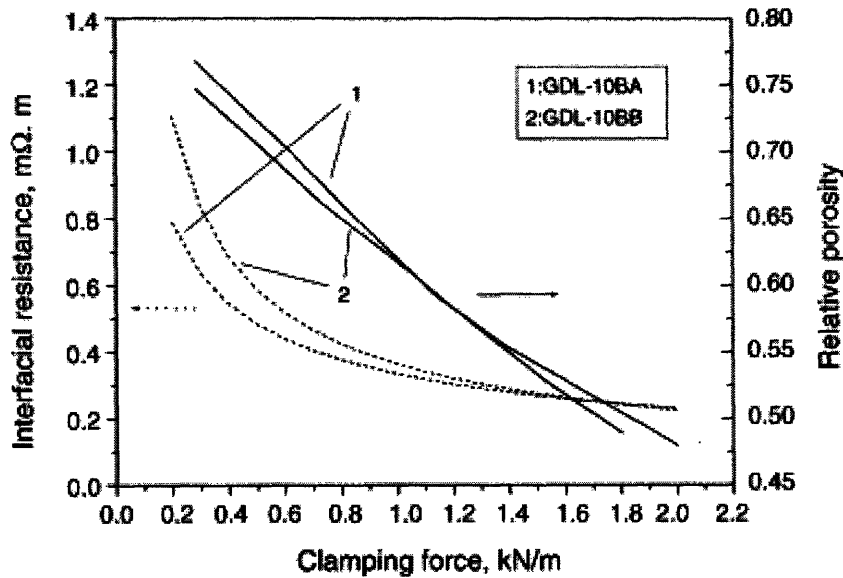


Figure 15. Relative changes in interfacial resistance and porosity as a function of clamping force for two different GDLs. The interfacial resistance decreases exponentially with force whereas the porosity drops off linearly over the same force range [29].

#### *Numerical and Experimental Characterization of PEM Fuel Cell Compression*

In contrast to examining the effect of compression on isolated components of a fuel cell, many research groups have studied the aggregated effects of compression by examining changes in the fuel cell power output [31, 34-38]. A summary of findings is presented in Table 2. In general, it is difficult to compare results between papers since each investigation used different fuel cell components, particularly different GDLs, and performed tests at different operating conditions. Therefore, the data in Table 2 should be interpreted cautiously and used only to develop a general sense for how performance changes with applied stress.

Reference	Analytical or Experimental?	Control Parameter	Stress Range Explored	Pressure at peak power
31	experimental	% compression of GDL	15-50%	unknown <sup>4</sup>
34	analytical	clamping stress	0.58-2.43 MPa	1.62 MPa for simulated GDL
36	experimental	bolt torque (pressure film used to correlate with stress)	100, 125, 150 in-lb/bolt	1.6 MPa for TORAY™ carbon paper; 9.3 MPa for ELAT® carbon cloth
37	experimental	bolt torque (pressure film used to correlate with stress)	0-5MPa	2 MPa for TORAY™ carbon paper
37	experimental	clamping pressure (method uncertain)	0.2-2 MPa	1-2 MPa for carbon cloth

**Table 2. Summary of stress-performance findings in the literature.**

### 2.2.2 Limitations of Previous Approaches

To date, almost all of the experimental techniques that have been used to quantify the compression – performance relationship have varied clamping force by moving the outer plates closer together or increasing the bolt torque. This is problematic for three reasons.

Firstly, since the gasket material and GDLs have different mechanical properties, it is unclear how the applied stress is distributed over the interior of the system. A stiffer material will absorb more of the applied stress than a less stiff material for a given

<sup>4</sup> The compression at peak performance is roughly 15% for both carbon cloth and paper, and for various flow rates. Note that in most cases 15% was the minimum compression that was possible given the sealing requirements.

displacement. Therefore, unless special techniques are taken to examine the internal pressure distribution (discussed below), there is no direct correlation between the applied stress and the actual stress seen by the GDL.

Secondly, in a typical fuel cell setup the outer plates must be held together with a minimum clamping pressure in order to achieve an adequate seal. This requirement limits the range of applied stress that can be explored experimentally. Since the contact resistance has been shown to change most dramatically at low magnitudes of clamping pressure, an experimental setup that cannot explore these low-stress regions may ignore some of the most interesting and useful features of electrode compression.

Finally, it is more useful from a design perspective to have a “universal” parameter (stress) to predict optimum performance since it can be applied to any fuel cell by considering the unique features of the system. In contrast, a system-specific parameter such as percent compression of the GDL is wholly unique to the system, and the information cannot be generalized for other setups.

The use of pressure-sensing films to correlate the internal pressure distribution with bolt torque is a step in the right direction towards a more comprehensive stress-performance model, but there are inherent limitations in the nature of these films that create a lack of confidence in their accuracy. Commercially-available pressure sensing films record only the maximum pressure that is applied over an arbitrary time range, and cannot provide information about how the stress might vary dynamically. To develop a correlation between the pressure and bolt torque, the pressure film is inserted into the fuel cell in typically dry conditions (prior to cell operation). The pressure that is measured reflects only the distribution at this particular instance in time. However, once a fuel cell begins running, the membrane hydration can vary dramatically on a time scale of many hours. Since the membrane is constrained between two stiff plates, the stress in the membrane will change during this time. Therefore, the stress state that was measured in the dry condition does not adequately capture the internal stress during hydrated operation of the cell.

In summary, in the experimental setups described here there is inherent coupling between force application/measurement and the need to seal the fuel cell. In order to fully examine the effect of compression on fuel cell performance, and to increase confidence in



the accuracy of the data, it is necessary to decouple these effects. It is also desirable to identify an alternative means of measuring the internal stress more accurately, and *in real time*, so that any changes in the fuel cell state are accounted for automatically in the stress measurement.

### **2.2.3 Questions to Answer about Fuel Cell Compression**

As was mentioned earlier, what matters most at the end of the day – the fuel cell power output – is affected by a complex web of engineering and operating parameters whose relationship is not easy to determine. Historically, investigations have examined some of these relationships *ex-situ* as though they were independently meaningful, for instance, by studying the effect of the clamping pressure on the contact resistance. However, this approach does not capture what is really happening in the fuel cell during operation when system parameters are more strongly coupled. The relationship between clamping pressure and contact resistance is not meaningful, then, unless it is examined at different operating conditions, and unless we consider its relative effect on the fuel cell power output.

There are a number of questions relating to fuel cell performance and design optimization which are as yet unanswered by the work in the literature:

- Which parameters (ICR, GDL porosity) dominate the fuel cell performance in a given stress range?
- What are the most significant design parameters that should be considered in fuel cell design, and does their importance vary depending on the stress range?
- Which component materials and morphologies lead to the highest power output for a given set of operating conditions and applied stress?
- Conversely, for a given system (with given materials and dimensions), what operating conditions should be selected to maximize performance, and how do the optimal conditions vary with applied stress?
- Is there an overall optimal stress range for all PEM fuel cells?

- How can this information, once acquired, be used to improve the fuel cell design process?

Historically, the fuel cell design process has been driven by much trial and error. As we look towards a future that is powered by alternative energy systems such as fuel cells, it is desirable to develop a more systematic approach to fuel cell design that can identify *a priori* the key considerations that a design engineer faces. Doing so requires a thorough understanding of the many factors that affect fuel cell performance and how they affect each other. Only with this complete understanding is an engineer fully free to maximize performance while meeting the constraints of the particular system at hand.

### **3.0 Design and Manufacture of a Decoupled Test Setup for Studying the Stress-Performance Relationship in PEM Fuel Cells**

The main thrust of this experimental work has been the design and manufacture of a fuel cell test setup that is capable of accurately measuring the effect of electrode compression on the fuel cell power output. It is believed that other experimental works that explore this relationship may not adequately decouple important system parameters, such as force distribution and sealing, and that this raises questions about the reliability of the data. The reason that this decoupling is not achieved is due to inherent design limitations of the test setups that were used. In order to improve confidence in the experimental data, a new setup was created by the author which specifically addresses the coupling concerns mentioned previously. Furthermore, this test setup enables a new type of fuel cell characterization in which an important operating parameter – mechanical stress – that has often been disregarded can be used to develop a more comprehensive fuel cell performance model.

#### **3.1 Design Requirements for a Decoupled System**

The limitations of previous attempts to study fuel cell compression, as outlined in Section 2.2.2, point clearly to a set of key features that an improved setup should have. These key features are defined here as *functional requirements* of the system and directly drove the design process. These functional requirements are:

- Applied stress must be constrained to the electrode area only. When force is varied over the active area, no additional force should be applied to the seal or surrounding membrane material.
- It must be possible to vary compressive force during testing without disassembling the setup.

- There should be no limitations on the range of compressive forces that can be explored experimentally.
- The sealing capability and quality must be independent of applied force.
- The compression parameter must be directly measurable and should be expressed as a “universal” term that can be interpreted usefully for any fuel cell system, rather than a system-specific measurement like percent compression. An ideal measurement parameter is compressive stress.

### 3.2 Presentation of Design

The author’s experimental setup is presented in Figure 16. The design consists of two main parts: the fuel cell functional unit (shown in purple/silver) and the outer case that is used to constrain the fuel cell and apply force. The uniqueness of the design is perhaps better understood after comparison with a traditional fuel cell test setup in which the clamping stress is not constrained to the electrode area.

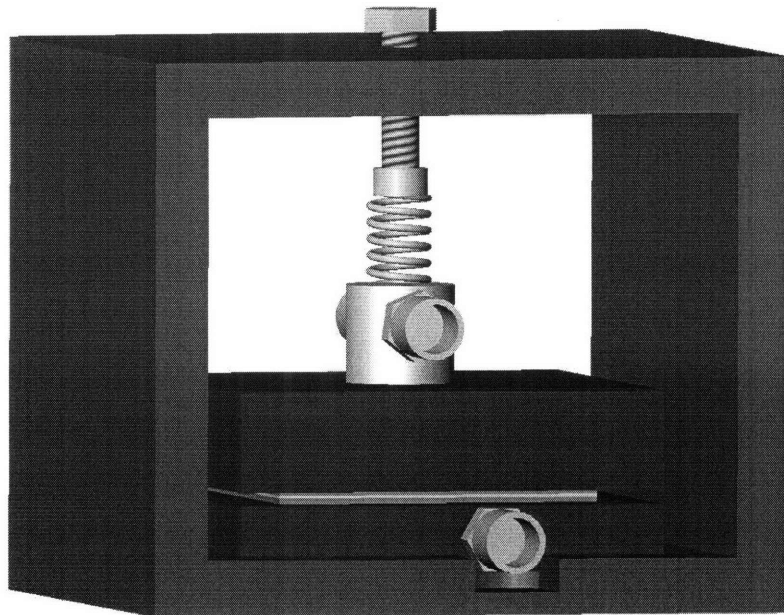
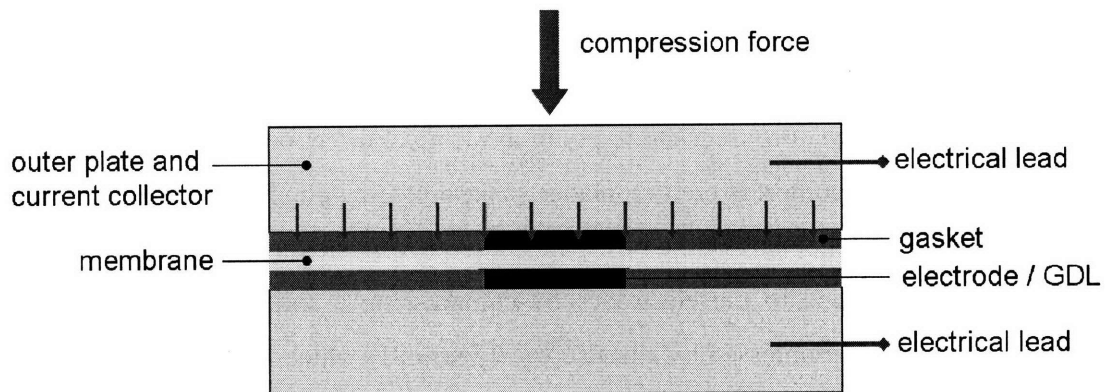


Figure 16. Improved compression-test design.

In a traditional fuel cell design (Figure 17), the MEA is clamped between two stiff, identical outer plates which distribute the fuel and oxidant to the electrodes and draw current from the cell. Current is generated in the electrode area of the MEA and flows through the outer plate to the electrical leads, where it is directed through an external load. In order to ensure that no gas escapes from the cell, a planar gasket (shown in blue) is placed between each side of the MEA and the respective outer plate. When the outer plates are bolted together tightly to form a seal, compressive stress is distributed over both the electrode area and the gasket material. However, only the electrode stress affects the electrochemical performance of the cell. Since a certain minimum compression force is required to seal the cell, the performance of the cell is directly coupled with the sealing requirement. To complicate matters further, the compressive stress is not necessarily uniformly distributed over the gasket and electrode, making it very difficult to accurately determine the electrode stress during cell operation.



**Figure 17. In a traditional fuel cell design, the compressive force that is necessary for sealing the cell is distributed over both the gasket and the electrode area; however, only the electrode stress affects the electrochemical performance of the cell.**

The author's design addresses the limitations of traditional fuel cell designs by separating the functionality of sealing and gas distribution/current collection into two components that can move relative to one another during cell operation (Figure 18). Current collection is accomplished by a cylindrical component with a rectangular base, referred to as the Adjustable Current Collector, or ACC, as shown in Figure 19. The ACC plays the role of a traditional outer plate by distributing the reactant gas to the electrode via a serpentine flow field (Figure 19b) and by drawing current from the electrode.

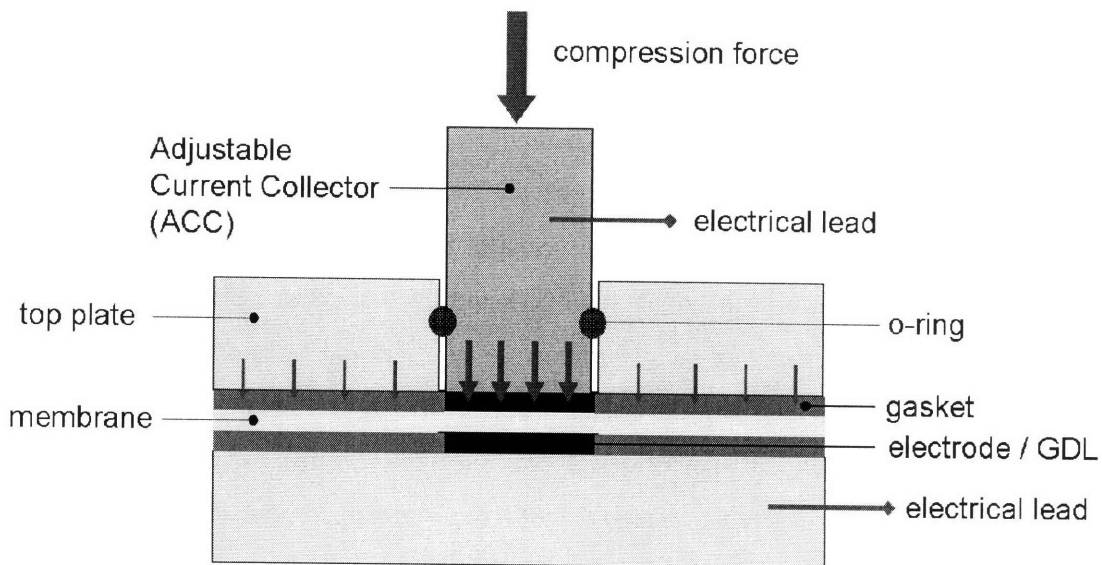


**Figure 18.** In the new setup, the sealing and current collection functions are decoupled. The Adjustable Current Collector (ACC) contacts the electrode and is free to translate vertically. The top plate only contacts the gasket; the stress that is applied to the electrode (shown in purple) is therefore completely decoupled from the stress required to seal the cell (shown in red). An o-ring located between the ACC and top plate provides a seal that is independent of ACC position.

A top plate fits around the ACC and is bolted to the bottom plate, which has the same form as in the traditional setup. The top plate has a cut-out feature that accepts the shape of the ACC and allows it to translate freely in the vertical direction. The sole function of this outer plate is to compress the two planar gaskets located on either side of the MEA. Figure 20 depicts a schematic of the flow paths of hydrogen and oxygen in the new setup.

Force is applied to the electrodes by compressing a spring that rests atop the ACC. The spring is compressed by a leadscrew (Figure 21) which is in turn supported by the outer case in which the fuel cell rests during operation. By measuring the deflection of the spring, the compressive force applied to the electrode area can be directly measured for any position of the leadscrew. The surface area of the bottom face of the ACC that is in contact with the top electrode is known and was chosen by the author prior to manufacturing, and therefore calculation of electrode stress is straightforward once the compressive force is measured.

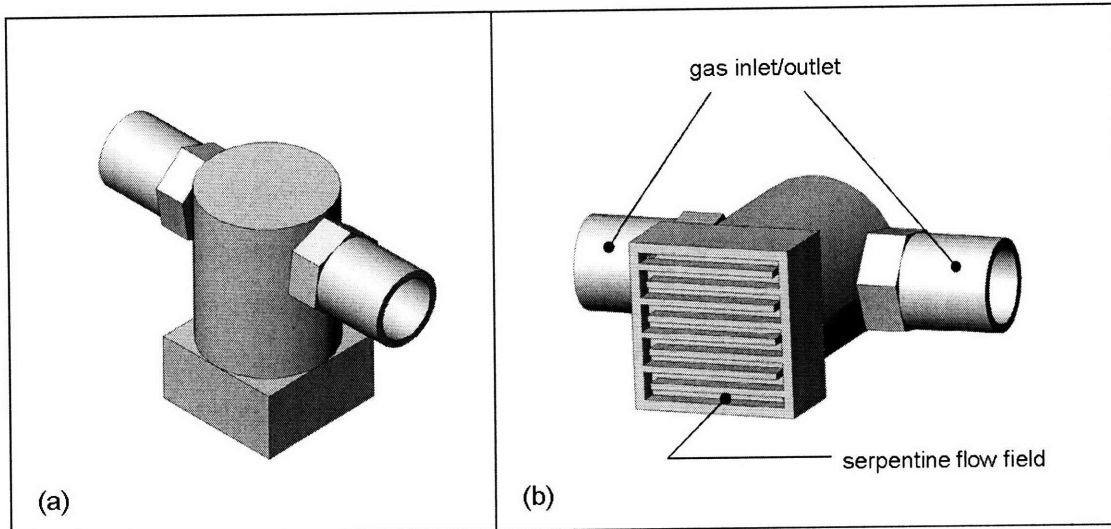


**Figure 19.** (a) The Adjustable Current Collector (ACC) performs the functions of gas distribution to the electrodes, current collection, and transmission of an externally-applied force to the electrode area inside the fuel cell. On the bottom face (b), the serpentine flow field directs the flow of hydrogen or oxygen over the electrode.

A key feature of this experimental setup is that the stress applied to the electrode area is completely decoupled from the stress required to seal the cell. Indeed, it is even possible to apply *no stress* to the electrode area while the cell is fully assembled and operational by moving the ACC vertically upwards so that it no longer contacts the electrode. Whereas a traditional design requires that a minimum stress be applied to the electrodes in order to seal the cell, the author's setup allows a full range of forces to be explored starting from 0 MPa. Figure 22 shows some photographs of the completed test setup.

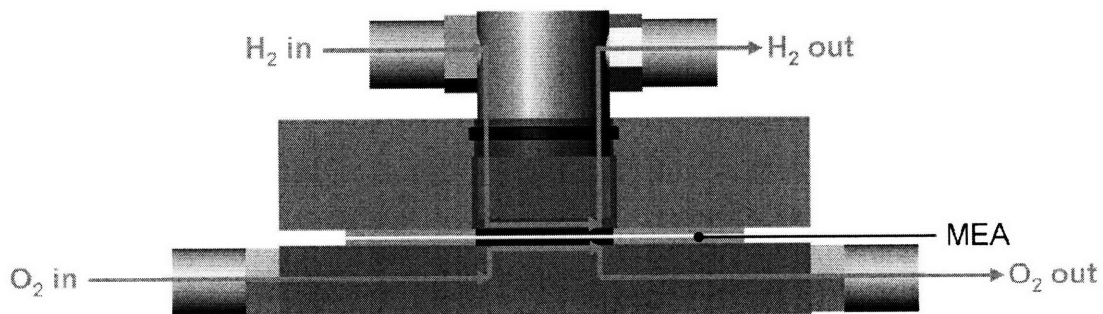


**Figure 20.** Internal flow paths for hydrogen and oxygen; gas separation is maintained by the presence of the polymer membrane (yellow) and gaskets (blue).

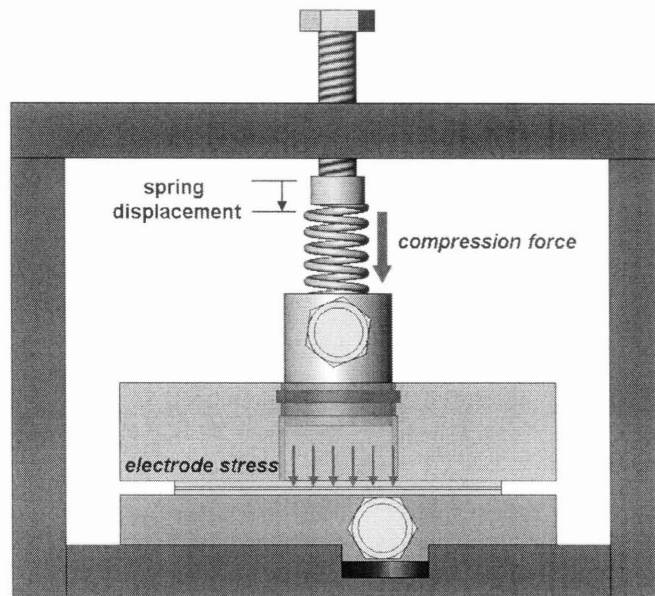


Figure 21. By turning the leadscrew that is supported by the outer frame, the spring displacement is controlled and compressive force is applied to the ACC. The applied force is transmitted as compressive stress to the electrode area directly below the ACC.

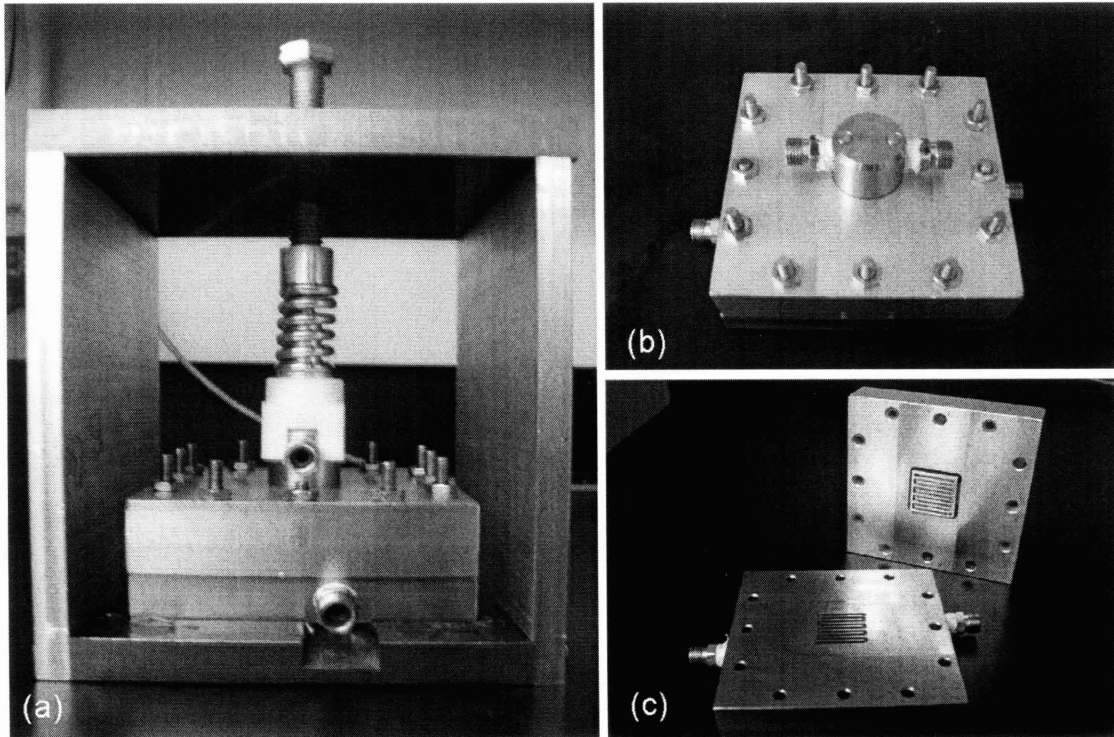


Figure 22. Pictures of the completed test setup: (a) The fuel cell supported in the outer case and under compressive load; (b) the functional fuel cell unit assembly; and (c) fuel cell disassembled to show the bottom plate (front) and the ACC/top plate assembly (back).



### **3.3 Unique Features of the Test Setup**

Examining a few key features of the improved test setup will help elucidate its functionality as well as highlight some new experimental methods which are now possible.

#### *Sealing*

Sealing between the perimeters of the two outer plates is accomplished in an analogous fashion to sealing in traditional fuel cell setups. However, the introduction of an additional part which must interface with the top plate and move relative to it (the ACC) has also introduced a new sealing requirement. This need was met by using an o-ring that is inserted between the top plate and the ACC, and which remains stationary in a groove that is machined into the top plate (Figure 18). The o-ring is compressed radially as the ACC is inserted into the top plate during cell assembly, and since the seal is radial, the quality of the seal is constant and independent of the vertical position of the ACC with respect to the rest of the cell. A further advantage is that the static friction between o-ring and ACC is straightforward to measure, and results in a constant additional force that acts against the spring to decrease the actual applied force by a fixed and predictable amount.

#### *Real-time Measurement Capability*

Fuel cell performance can be sensitive to the conditioning history, meaning that the power production at any instant is dependent upon the history of hydration, water production and removal in the cell. Disassembling and reassembling the cell between tests can disrupt the equilibrium state of the fuel cell and introduce undesirable variables into the experiment. In order to detect performance changes due to compression only, it is necessary that the force be varied without disassembling the cell and that it be measured in real time. The author's setup allows force to be swept through a wide range and for the force application mechanism to be changed if desired, all without disassembling the functional unit of the fuel cell.

### *Modularity of Design*

The ACC was designed to perform as a modular component that can be easily interchanged with other ACCs having different material and morphological properties. For instance, to study how different values of Interfacial Contact Resistance affect peak power and optimal applied stress, an ACC with the same flow field dimensions but made of a different material can be manufactured. Alternatively, one could study the effect of changing the flow field dimensions while keeping the current collector material the same. The test setup allows a researcher to systematically explore the effect of changing only one engineering parameter and directly observing if and how the peak power and optimal stress vary. The ability to obtain this type of information is very useful and allows an engineer to optimize the fuel cell performance when faced with particular design constraints.

### *Tuning of Measurement Sensitivity*

Since the spring deflection is measured visually, the sensitivity of the force measurement is determined by the stiffness and length of the spring. For instance, for a very stiff spring, a small deflection can yield a large  $\Delta F$ , whereas for a spring with low stiffness, a larger deflection can be applied for the same  $\Delta F$ . However, the measurement limitation is the same for both cases and is determined simply by how accurately the human eye can detect changes in deflection. Therefore, the spring with lower stiffness will allow more fine gradations of force to be explored, while the stiffer spring is optimal for making large step changes in the applied force.

### *Range of Stress That Can Be Explored*

A specific objective of this design was to decouple the force application from the need for sealing. Since sealing is achieved radially through an o-ring, the seal quality is unaffected by vertical translation of the ACC and is truly independent of the ACC position. Therefore, unlike in other setups, it is possible to draw current from the fuel cell at essentially 0 MPa of applied force – when the ACC is just barely in contact with the GDE. It is also possible to achieve OCV even when the ACC is not in contact with the GDE since the planar seal successfully constrains the inlet gas to the electrode area only.

The only upper limitation to the magnitude of compression force that is possible is the physical limit that the MEA can withstand before destruction occurs.

#### *Versatility*

Since the compressive force is actuated externally, any variety of force actuators could in theory be used. So far, simple compression springs have been used because they offer certain important advantages: they are inexpensive and readily available commercially. Furthermore, springs are available in a wide range of stiffness for a given general size. This means that, with relative ease, springs can be switched out at a moment's notice in order to explore a wider range of stress. Additionally, the sensitivity of the force measurement can be fine-tuned by using springs with different stiffness-to-length ratios, as discussed above. If greater data accuracy were desired, an electronically controlled force actuator could be easily integrated into the system with very few changes to the setup, and with virtually no changes to the functional components of the fuel cell.

In previous investigations in the literature, pressure sensing films were used to correlate the outer plate bolt torque with the internal stress. As discussed earlier, these correlations were made when the fuel cell was in the dry, non-operational state and it is possible that the actual internal stress in the hydrated, operational state is much higher. In the manner in which they are presented in the literature, previous test setups are unable to account for a varying stress state inside the fuel cell.

In contrast, in the present setup, the spring deflection at any instant in time during fuel cell operation both applies and *indicates* the compressive stress acting on the electrode area. Since the force can be varied in real time, the opposite also holds true: the force can be *detected* in real time. Therefore, any changes in the internal stress state are observable and the applied force at any time reflects the true internal state of the fuel cell.

### **3.4 Selection of Material and Morphological Parameters**

#### *Material Selection*

A fuel cell environment is known to be corrosive under certain operating conditions, particularly when large amounts of water are produced and remain in the cell [39].

Therefore, it is important that the materials directly in contact with the reactant gases and electrodes (i.e., the outer plates and current collectors) exhibit sufficient corrosion resistance. This is part of the reason why graphite is typically used as a current collector material in PEM fuel cells. Various works [18, 19] have examined the susceptibility of various metals to corrosion in a fuel cell environment. The findings show that, compared with other metals like aluminum, stainless steels and some coated metals provide satisfactory corrosion resistance in the long term and could be viable alternatives to graphite.

Since graphite is quite brittle, and therefore difficult to machine, stainless steel grade 316 was used for both the ACC and outer (bottom) plate. 316 is known to be one of the most corrosion-resistant grades of stainless steel and performs well over many hundreds of hours of testing. Additionally, stainless steel is relatively inexpensive and easy to obtain commercially. The choice of current collector material has a large effect on the fuel cell performance and determines both the interfacial and bulk resistances of the system, as well as heat management capability.

#### *Electrode (Active Area) Size*

An active area of 5 cm<sup>2</sup> was selected for new setup. Generally, when designing a fuel cell for commercial use, the active area will be 25 cm<sup>2</sup> or 50 cm<sup>2</sup> since the total power of the cell scales roughly with the size of the electrodes. In this study, the objective is not to design a cell that produces as much power as possible, but rather to design a test setup that can help elucidate the effect of *changes* of both engineering and operating parameters on fuel cell performance. An active area of 5 cm<sup>2</sup> is sufficient for this purpose and also conserves the amount of material needed for the design. However, if it were ever desirable to do so, this design could easily be scaled up to accommodate a larger active area in order to explore how performance scales with size.

#### *Flow Field Dimensions*

Various works in the literature [26, 40] have shown that the dimensions of the flow field, particularly the ratio of flow channel width to rib spacing, can have a significant impact of the fuel cell performance. The design of a flow field reflects key tradeoffs between

how much fuel or oxidant can access the cell, how much pressure is lost as the gases flow from inlet to outlet over the electrode, and how much surface area is in contact with the electrode in order to conduct current away from the cell. The ideal ratio of flow channel to rib spacing will depend somewhat on the material and operating parameters.

Since the fuel cell test setup was machined by the author, certain constraints were faced when designing the serpentine flow field. For instance, stainless steel is quite difficult to machine since it work hardens, and therefore, given the dimensions of the bottom face of the ACC, it was not possible to machine a flow field having less than 50% flow channel surface width. Therefore, the author designed a flow field that has 50% flow channel and 50% rib contact area. The percentage of rib contact area in the author's setup is large compared to that of a conventional serpentine flow field which is typically closer to 75%. This difference could create higher ohmic losses in the author's setup and may also affect the pressure of oxygen and hydrogen along the flow channel. The implications of high ohmic loss will be discussed in following sections.

## **4.0 Experimental Approach**

### **4.1 Selection of Operating Parameters**

The objective of this work was to characterize how the fuel cell performance changes as a function of applied stress for a variety of operating conditions. Specifically, it was desirable to see if increasing the applied stress helps or harms the fuel cell performance and to identify the “best” operating stress range for given conditions. This study examined the effect on fuel cell performance of varying the following operating conditions:

- Electrode stress
- Cell temperature
- Cell backpressure

The anticipated effects of varying these operating parameters was discussed in Section 2.1.7.

### **4.2 Cell conditioning**

In order to ensure full hydration of the membrane and stable cell operation during data collection, a standard conditioning procedure was implemented for all tests:

- The cell was fully assembled and electrode stress was set to a pre-determined fixed value.
- A lifetime test was performed in which the cell voltage was held constant at 0.3 V and the current density was recorded as a function of time in response to a step change in operating conditions. An exponential rise in the current density with time was consistently observed, and the current density showed a

leveling-off after 1-2 hours that indicated an approach to steady-state behavior.

- Once steady-state behavior was observed, the lifetime test was stopped and voltage-current (V-I) tests were run. The cell was cycled from 0.95V to 0.1V repeatedly until the current density at a given voltage (typically 0.3 V) did not change by more than 10 mA/cm<sup>2</sup> between tests. After this point, the cell was considered to have reached steady-state for the particular value of applied stress.

### 4.3 V-I Curves

The process outlined in 4.2 was repeated for many different force values ranging from 0.8 MPa to 4.4 MPa. Each time the applied force was changed, lifetime and break-in tests were run to monitor the cell's performance and to determine when the cell had reached steady state prior to data collection.

For most tests, force was swept from high to low values (4.4 MPa to 0.8 MPa) for two reasons. Firstly, since compression generally enhances the cell current generation, the membrane became hydrated much more quickly at higher force and the time for the cell to reach an equilibrium state was greatly diminished. Secondly, since it is possible that high forces cause damage to the MEA, sweeping from high to low force would cause this damage to be during conditioning and would affect the performance roughly equally at all lower force values. This scenario was deemed preferable over possibly doing damage only at the high end of the force range (such as when sweeping from low to high force), which could prevent useful comparison of the V-I curves at the different force values. For operation at higher cell temperature, however, the effect of mass transport was so severe at high force that the GDL quickly flooded and stayed that way, preventing useful data from being collected at lower force. Therefore, for the highest temperature only (65°C), force was swept from low to high to avoid critical, irreversible flooding.

## 4.4 Electrochemical Impedance Spectroscopy (EIS)

### 4.4.1 Overview: Information Gained from EIS

Electrochemical Impedance Spectroscopy, or EIS, is an experimental tool that is used to probe the electrochemical mechanisms that affect fuel cell performance and that occur on different time scales. In EIS, a small AC current or voltage perturbation of the form  $V(t) = A_v \sin(\omega t)$  or  $I(t) = A_i \sin(\omega t)$  is input into fuel cell and the resulting current or voltage response, respectively, is measured. Since the input signal is oscillatory, the response signal takes a different magnitude than the input as well as a phase shift  $\phi$  and will therefore have both real and imaginary components. By exciting the system at a range of different frequencies, certain mechanisms can be “selected” when the input is on the scale of the relevant characteristic frequency of the mechanism. For instance, electrode kinetics, which occur with relatively high frequency [41], are excited when the input frequency is high; in contrast, mass transport effects, which occur on a longer time scale than that of the electrode kinetics, are best detected when the input frequency is low.

### 4.4.2 EIS for a PEM Fuel Cell

A number of works [41-44] have studied the AC impedance response for a PEM fuel cell and have identified key features that appear consistently in almost all fuel cells. A summary of these features appears in Figure 23. In a model proposed by O’Hayre et al. [41], information about the fuel cell system may be interpreted from AC impedance data in the following manner:

- *High-frequency intercept.* The intersection of the AC response curve with the real axis at high frequency gives the total ohmic resistance,  $R_\Omega$ , of the experimental setup. Ohmic losses include bulk resistance in the current collectors, interfacial resistances and the protonic resistance in the membrane.



- *Size of high-frequency semi-circle.* The size of the higher-frequency semi-circle is indicative of the kinetic (also known as Faradaic) losses at the anode. The diameter of this semi-circle is identified in Figure 23 as anodic Faradaic resistance,  $R_{f,A}$ .
- *Size of lower-frequency semi-circle.* The size of the lower-frequency semi-circle reveals the magnitude of kinetic losses at the cathode. Since cathode losses make up the bulk of the total activation overpotential in a PEM fuel cell, in AC impedance the cathode features tend to dominate and even dwarf the anode features. In fact, sometimes the cathodic losses are so dominant that the two semi-circles combine and only one large semi-circle is observed.
- *45° branch at high frequency.* A 45° branch where the AC curve first leaves the real axis at high frequency is indicative of insufficient membrane hydration and insufficient protonic conductivity.
- *Presence of low-frequency “tail.”* After the conclusion of the second semi-circle at low frequency, the curve will sometimes branch off to infinity, resulting in a “tail”-like feature. This feature is attributed to poor mass transport caused by insufficient water removal from the cell or by low porosity in the GDE. In general, this feature is only observed in systems with severe mass transport limitations such as air cathodes, and is less frequently seen with cells that use oxygen as the oxidant.

The shape of the AC impedance response depends upon the DC bias voltage around which the perturbed input signal oscillates. Figure 24 illustrates the effect of performing AC impedance at different points along the V-I curve. At high voltage close to OCV, the activation overvoltage is small and the kinetic losses are large. Therefore, the kinetic features (semi-circular features) in the AC impedance plot should dominate the behavior at all frequencies (Figure 24a). At an intermediate voltage of 0.6 V, the driving force for electrode kinetics is higher due to a larger overpotential and mass transport effects have not yet started to dominate. Therefore, the size of the semi-circle decreases while the overall shape of the curve stays the same (Figure 24b). At low

voltages (Figure 24c) where mass transport is limited, the low-frequency “tail” becomes apparent. The overall size of the semi-circular region is smaller yet due to even higher driving overpotential for the electrode kinetics. Note that the high-frequency intercept at  $R_{\Omega}$  is fixed regardless of the DC bias, as one should expect since it is not a dynamic process and is independent of excitation frequency.

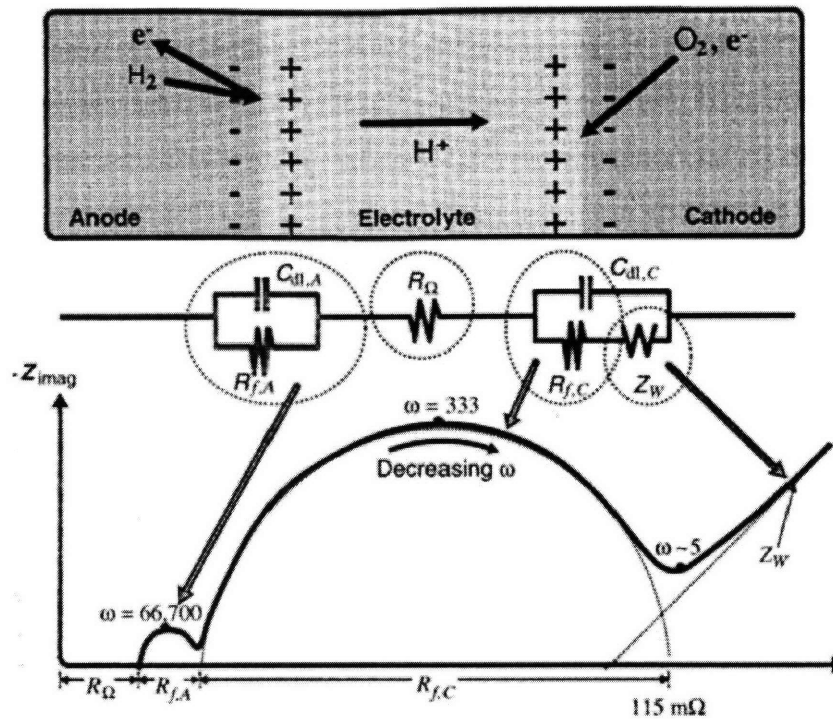


Figure 23. Typical electrochemical impedance response for a PEM fuel cell. At high frequency, the real-axis intercept represents the total ohmic resistance of the cell. The sizes of the semi-circles scale with anode and cathode kinetic losses and the low-frequency tail indicates mass transport limitations [41].

Although the O’Hayre et al. model predicts a shrinking semi-circle with decreasing DC bias, Springer et al. [42] found that in cells with significant mass transport losses, the semi-circle will instead grow with decreasing voltage. Since these trends are conflicting, neither of these two models should be applied blindly when interpreting EIS data for a PEM fuel cell. Instead, it is necessary in practice to correlate EIS data with other data, such as DC current-voltage information, in order to determine whether mass transport effects do appear to be significant or not.

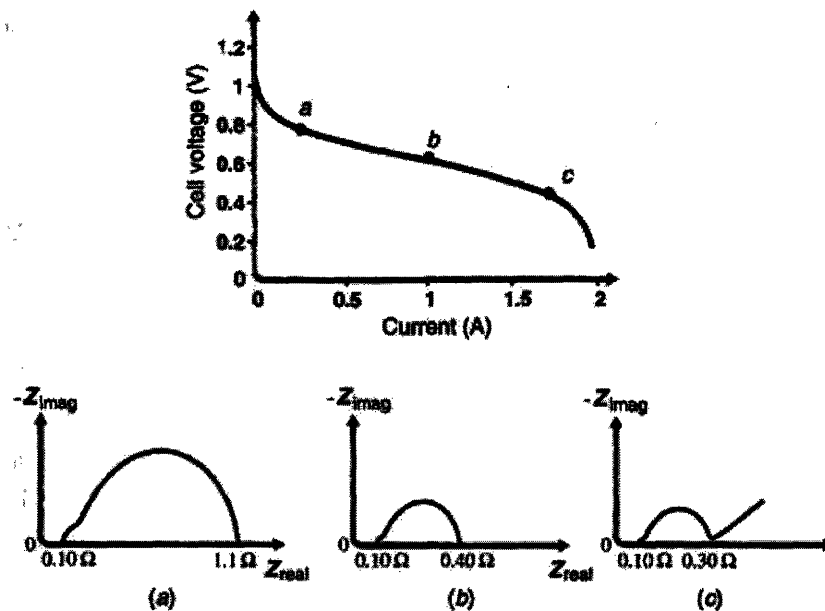


Figure 24. The shape of the impedance-response curve depends on the operating cell voltage (overpotential). (a) At high voltage (low overpotential), the response is dominated by sluggish kinetics as evidenced by the relatively large diameter of the semi-circle. (b) At intermediate voltage and overpotential, the reaction kinetics are improved and the semi-circle is smaller. (c) At low voltage (high overpotential), the electrode kinetics are still faster and a low-frequency “tail” feature indicates mass transport limitations [41].

#### 4.4.3 Use of EIS in this Study

Electrochemical impedance was used in this study to help verify the changes in performance due to compression that were observed using the author’s setup, and as an alternative and complementary tool for better understanding the cell processes that were affected by applied force. For a given force, AC impedance was performed at three DC cell voltages (0.8V, 0.4V and 0V) which were selected due to the expected predominance of different loss mechanisms (activation, ohmic and mass transport losses, respectively) in each regime. Two representative force values, “low” (1.6 MPa) and “high” (4.0 MPa), were explored for each operating condition. The AC response for the author’s setup was interpreted by comparison with Springer’s experimental results and with the model for a PEM fuel cell presented in [41].

## 4.5 Testing for MEA Degradation

Any test in which an MEA is exposed to cyclical thermal, hydro- or mechanical loading, such as the experimental work performed here, could potentially lead to long-term degradation and instability of the MEA. Two major concerns are irreversible damage to the porous GDE structure and creation and growth of pin-holes in the membrane that could lead to fuel mixing across the membrane. It is necessary to ensure that significant degradation in the MEA does not occur during testing so that the stress-performance data can be interpreted accurately and meaningfully.

In order to ensure that degradation did not occur, a degradation check was performed every three test sessions in which the performance was compared to a pre-established baseline performance of the same pristine MEA when it was first used in the fuel cell. The degradation test consisted of a lifetime start-up test, where the MEA was held at 1.6 MPa and 0.3 V until a stable current density was reached; several V-I tests at the same compression; and repetition of the prior two steps for a higher force value of 4.0 MPa. If, at the end of the degradation check, it was determined that significant, irreversible damage had occurred, the MEA was rejected and a fresh one was used thereafter.

## 4.6 Error Analysis

The most significant source of uncertainty is due to the fact that spring displacement is read by eye. The accuracy of this form of measurement was judged to be within 0.5 mm; since the spring constant was large (148.6 kN/m)<sup>5</sup>, the resulting uncertainty in the applied stress is 0.2 MPa at all stress magnitudes. At compression below 1.6 MPa the percent uncertainty is on the order of 20-25%, however, at larger magnitudes of stress, the percent uncertainty is significantly lower, around 5-10%. To account for the uncertainty, stress was applied in increments of 0.8 MPa so that the uncertainty ranges around each data point did not overlap.

---

<sup>5</sup> The spring stiffness was measured using an Instron and it is assumed that any inaccuracy in stiffness measurement is negligible.

## 5.0 Experimental Results and Discussion

### 5.1 Effect of Applied Stress on PEM Fuel Cell Performance

A representative set of V-I curves for a range of applied stress values is shown in Figure 25 for a cell operating at room temperature. At low stress magnitudes (less than 2.4 MPa), increasing the electrode stress had a significant effect on the maximum current density, with the largest gain occurring between 0.8 and 1.6 MPa. However, at larger stress magnitudes, the gains from increasing the applied stress were much less significant, and indeed the performance was virtually identical at both 4.0 and 4.4 MPa.

The V-I curves overlap at voltages above 0.85V, where activation losses tend to dominate cell performance, and then start to deviate once significant current is drawn from the cell at around 0.8 V. The absence of any clear mass-transport features (indicated by a steep drop-off in voltage at high current density, as in Figure 7) suggests that the cell performance was governed by ohmic losses at voltages lower than 0.8 V. The slope of the V-I curves becomes less negative with increasing stress, indicating that the ohmic losses in the cell are significantly reduced with compression.

The cell power density was obtained by multiplying voltage and current at each data point given in Figure 25. The resulting P-I curves are shown in Figure 26a for the same range of applied stresses. As with the V-I curves, increasing the applied stress had the biggest impact on performance at lower stress magnitudes, and there was little or no additional gain when stress was increased beyond roughly 4.0 MPa.

A plot of peak power density vs. applied stress (Figure 26b) was created by finding the maximum of each curve in Figure 26a. The peak power density increased monotonically with applied stress, with the largest gains at low stress magnitude (0.8 – 2.4 MPa). As stress increased to 4.4 MPa, the gains in peak performance leveled off and the peak power density approached a constant value of 210 mW/cm<sup>2</sup>. This is contrary to some of the results in the literature which show an increase, peak, and then decline in the power density as a function of stress (Table 2). Additionally, the peak power density reported in the literature tends to occur in the range of 1-2 MPa, which is significantly less than the range of stress explored in this work. This discrepancy may arise from

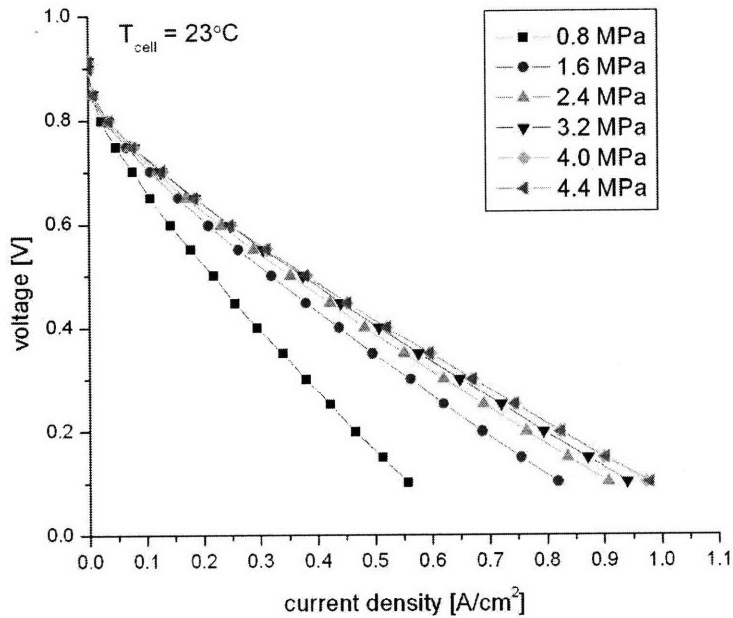


Figure 25. V-I curves as a function of applied stress for a cell operating at room temperature (23°C) and 0 psi gas backpressure. Flow rates: 90 cc/min anode, 75 cc/min cathode. 100% relative humidity of inlet gases.

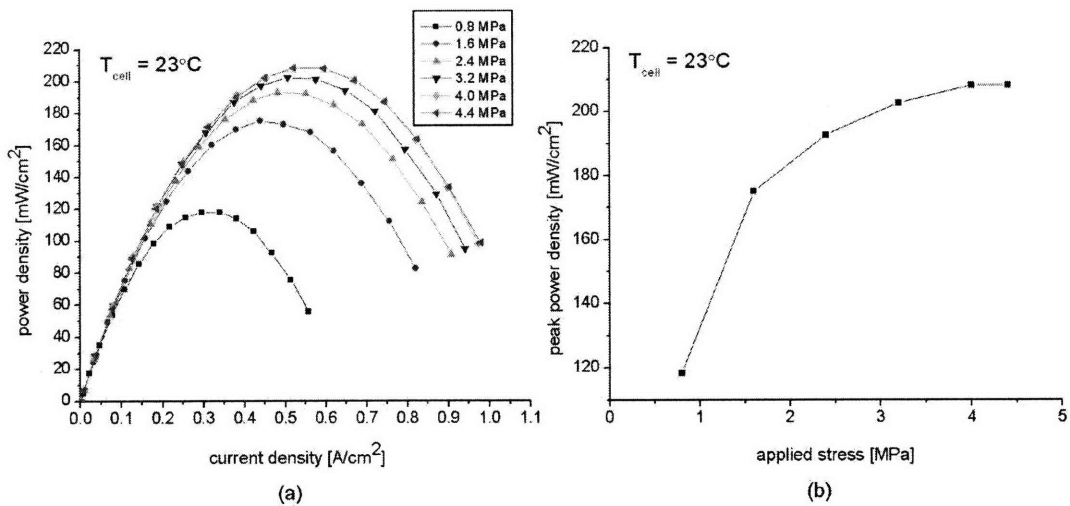


Figure 26. Performance characterization as a function of applied stress for a cell operating at room temperature (23°C) and 0 psi gas backpressure. (a) Power density curves for 0.8-4.4 MPa. (b) Peak power density as obtained from (a) as a function of applied stress. Flow rates: 90 cc/min anode, 75 cc/min cathode. 100% relative humidity of inlet gases.

inaccurate measurement of applied stress in other experimental setups; it may be that the stresses were actually much higher than believed, and that this led to early degradation of performance. Although it was not explored in this work, it is likely that if stress were increased much beyond 4.4 MPa, ultimately performance would start to decline due to mechanical degradation of the MEA.

For a fuel cell operating at room temperature and with the inlet gases at atmospheric pressure (no backpressure), Figure 26b suggests that cell performance is optimized at 4.0-4.4 MPa. However, this plot does not take into account the potentially harmful long-term effects of operating at high electrode compression. It is possible that an electrode stress of 4.4 MPa could harm the long-term stability of the cell by hastening the process of mechanical degradation that is already one of the biggest challenges to fuel cell commercial success. A fuel cell design engineer, then, could use Figure 26b, along with careful consideration of how stress affects cell lifetime, to determine an ideal stress that balances these tradeoffs and best suits the particular needs at hand.

In addition to the peak power, a second parameter of interest is the voltage at which peak performance occurred as a function of applied stress. Figure 27 depicts power-voltage (P-V) curves for the same range of stresses already presented. From this figure, it is clear that for the given operating conditions, the peak power occurred in the range 0.3-0.5V for all stress values. At 0.8 MPa, the power-voltage curve is much flatter at peak performance compared to the curves at 4.0 and 4.4 MPa, suggesting that performance at higher stress is more sensitive to selection of operating voltage than at lower stress.

The performance that is obtainable from this fuel cell setup at room temperature and at low compression is comparable to other values reported in the literature [45, 46] in which typical values of maximum current density for low-temperature operation fall between 0.6-0.8 A/cm<sup>2</sup>. At applied stress above 2.4 MPa, the peak current densities achieved with this test setup are competitive with other recent developments in the literature for low-temperature operation of PEM fuel cells. This fact suggests that the high stress ranges explored in this work may be beyond the range of typical clamping stresses used in traditional fuel cell setups.

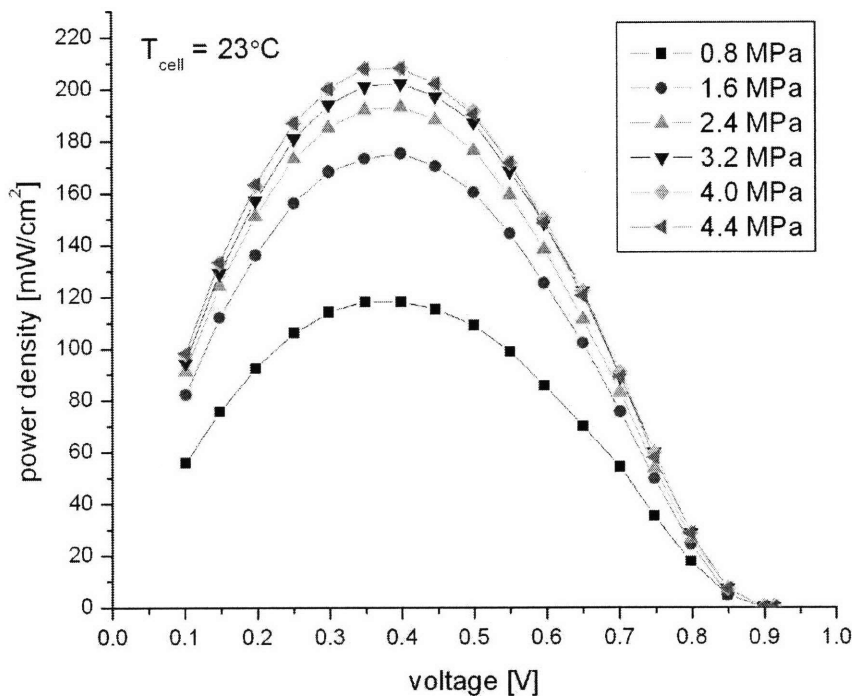


**Figure 27.** Power density as a function of voltage and applied stress for a cell operating at room temperature (23°C) and no inlet gas backpressure. Flow rates: 90 cc/min anode, 75 cc/min cathode. 100% relative humidity of inlet gases.

## 5.2 Effect of Backpressure on Stress-Performance Relationship

The data analysis described above was repeated for several different cell conditions in order to study how the stress-performance relationship depends on operating parameters. Sets of V-I curves as a function of stress were obtained for inlet gases pressures of 0, 10 or 20 psi, with all other operating parameters unchanged. A comparison of the V-I curves obtained at different backpressures for 1.6 MPa applied stress is depicted in Figure 28a, and the corresponding P-I curve appears in Figure 28b (for the full set of V-I curves, please refer to Appendix A).

At 1.6 MPa applied stress, increasing the backpressure from 0 psi to 10 psi or 20 psi improved the performance at low current density, where activation losses dominate the cell performance. This behavior is expected (see Section 2.1.7) since higher gas



pressure improves the hydrogen and oxygen coverage at the catalyst sites and helps facilitate the reaction kinetics. At high current density, however, increasing the backpressure had a detrimental effect on the cell performance, with the worst performance occurring at 10 psi. The shapes of the curves at high current density suggest that mass transport limitations were significant at higher pressures. Figure 28b shows that despite the apparent mass transport limitations, operating at 20 psi gave the overall best performance in terms of peak power density. However, at high current densities, the data suggest that it is preferable to operate without any backpressure. Interestingly, the intermediate 10 psi backpressure yields the worse performance at high current density.

When electrode stress was increased from 1.6 MPa to 4.0 MPa, the current density increased roughly proportionally for all values of backpressure (Figure 29a). However, the performance at 10 psi also improved with respect to the other two values of backpressure, making it the best, rather than the worst, operating condition at 4.0 MPa. Figure 29b shows that while the crossing-over of the 0 psi and the 20 psi curves still happens at intermediate current density, the performance at 10 psi has improved for all current densities.

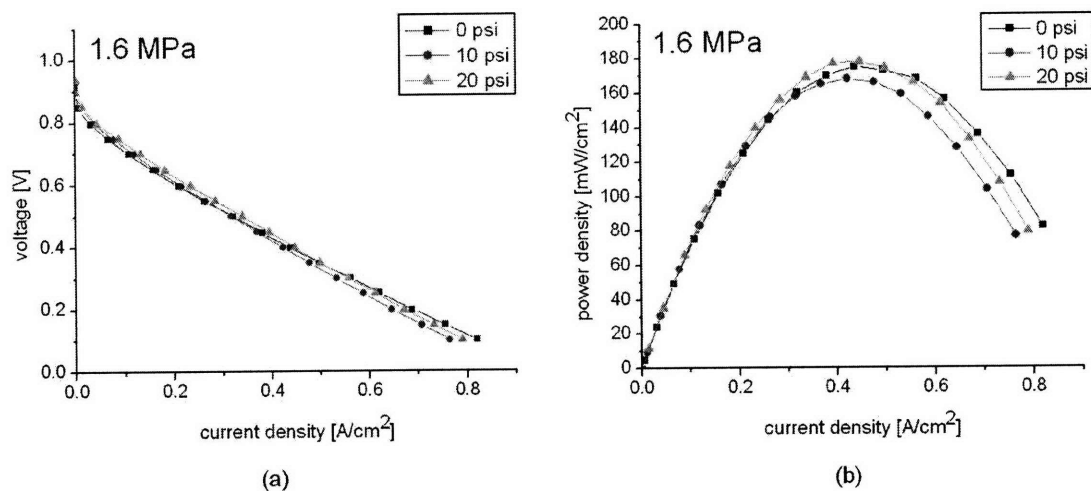


**Figure 28. Effect of backpressure on (a) voltage-current and (b) the power-current curves at 1.6 MPa for a cell operating at room temperature (23°C). Flow rates: 90 cc/min anode, 75 cc/min cathode. 100% relative humidity of inlet gases.**

A plot of peak power density vs. stress for the three values of backpressure is shown in Figure 30. From this figure it is clear that there is no advantage to pressurizing the inlet gases at low applied stress, but that at higher compression, either 10 psi or 20 psi are desirable depending on the stress magnitude. It is possible that below 1 MPa, the contact resistance is so high that it is not possible to take advantage of any improvements in reaction kinetics that occur due to pressurization of inlet gases. On the other hand, at higher stress the ohmic resistance is minimized so that performance is limited by kinetics and mass transport. The trade-off between 10 psi and 20 psi for optimal performance at high electrode stresses could reflect the chain-reaction that often occurs when fuel cell kinetics are enhanced: more current and therefore more water are generated and performance is initially improved, however, if the cell cannot remove this water quickly enough, the overall performance will degrade as a result of electrode flooding.

It is clear that at all stresses above 1.0 MPa, performance is maximized by pressurizing the inlet gases. Why then shouldn't all fuel cell systems operate at as high a pressure as possible, in order to take advantage of this fact? The answer is that the gains obtained by increasing backpressure may be entirely offset by the power required to pressurize the gases in the first place. Indeed, the maximum possible increase in power density achieved by increasing backpressure was 11% at 4.2 MPa, and depending on the system size and scale, this may not be enough to justify the need for more complicated,

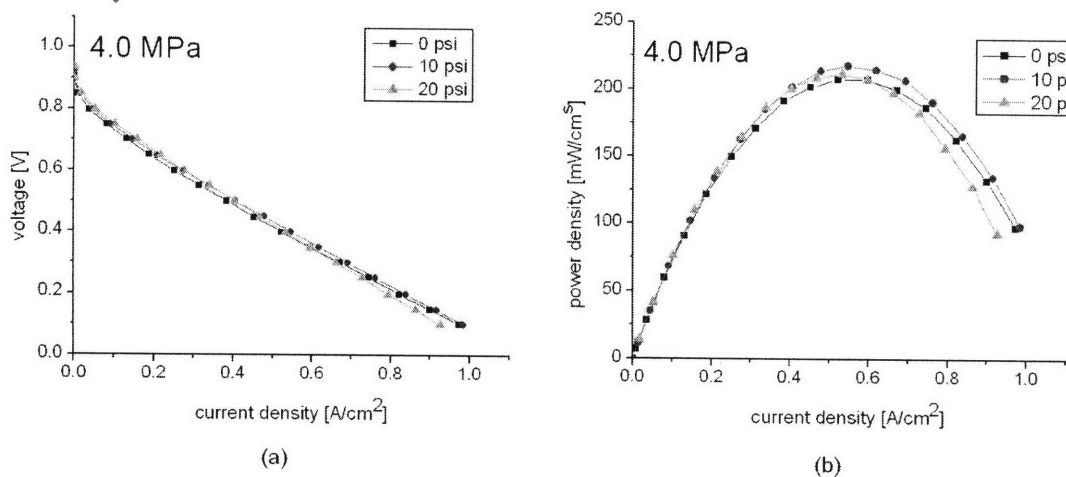


**Figure 29.** Effect of backpressure on (a) voltage-current and (b) the power-current curves at 4.0 MPa for a cell operating at room temperature (23°C). Flow rates: 90 cc/min anode, 75 cc/min cathode, 100% relative humidity of inlet gases.

expensive and power-demanding pressurization equipment. A fuel cell design engineer could use the stress-performance data presented here to weigh the costs and benefits of pressurization at different values of electrode stress in order to choose the best operating conditions for the cell.

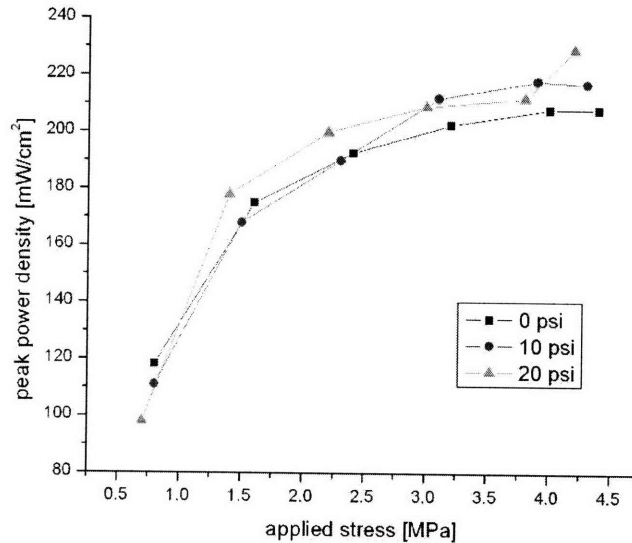


**Figure 30. Effect of backpressure on the peak power density as a function of applied electrode stress.**

*Voltage at Which Peak Power Occurred*

The power density as a function of voltage is plotted in Figure 31 for three values of applied stress at 10 psi. The absolute peak performance occurred at 0.4 V regardless of the applied stress, however, it is evident that electrode stress affected the overall shape of the P-I curves. Again, the curve at 0.8 MPa is much flatter at peak power density than the curve at 2.4 MPa, which is in turn flatter than at 4.0 MPa. In other words, at low stress magnitudes, there is little change in overall power density for a range of 0.35-0.45 V, whereas performance decreases more significantly over this same range for higher stress magnitudes. At high stress, then, it is more important to precisely select the desirable operating voltage in order to maximize performance.

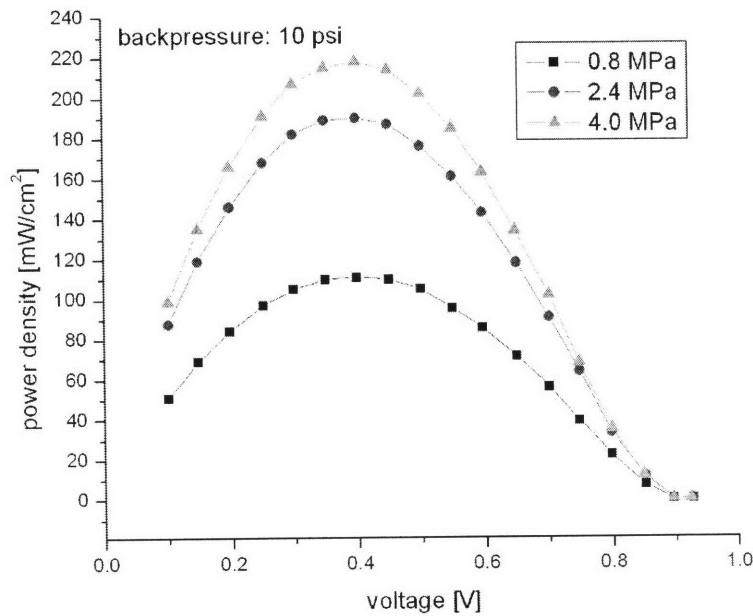


**Figure 31.** Power density as a function of voltage and applied stress for a cell operating at room temperature (23°C) and 10 psi gas backpressure. Flow rates: 90 cc/min anode, 75 cc/min cathode. 100% relative humidity of inlet gases.

### 5.3 Effect of Temperature on Stress-Performance Relationship

The relationship between operating temperature and cell performance is shown in Figure 32. Considering that the decline in cell voltage at low current densities corresponds to kinetic losses at the electrodes, it is clear that increasing the cell temperature from 23°C to 45°C improved the electrode kinetics and the overall cell performance at low current. At high current density, the slope of the 23°C V-I curve approaches a steeper (more negative) value than the slope of the 45°C curve. Since applied stress, and therefore contact resistance were held constant for this set of tests, and since it is unlikely that the bulk resistance of the current collectors changed significantly in this temperature range, the less steep slope may indicate that the ionic conductivity of the Nafion increased between 23°C and 45°C. As shown in Figure 32b, the peak power density at a constant applied stress of 1.6 MPa increased from 117 mW/cm<sup>2</sup> to 167 mW/cm<sup>2</sup> as temperature increased, resulting in a net performance gain of 43%.

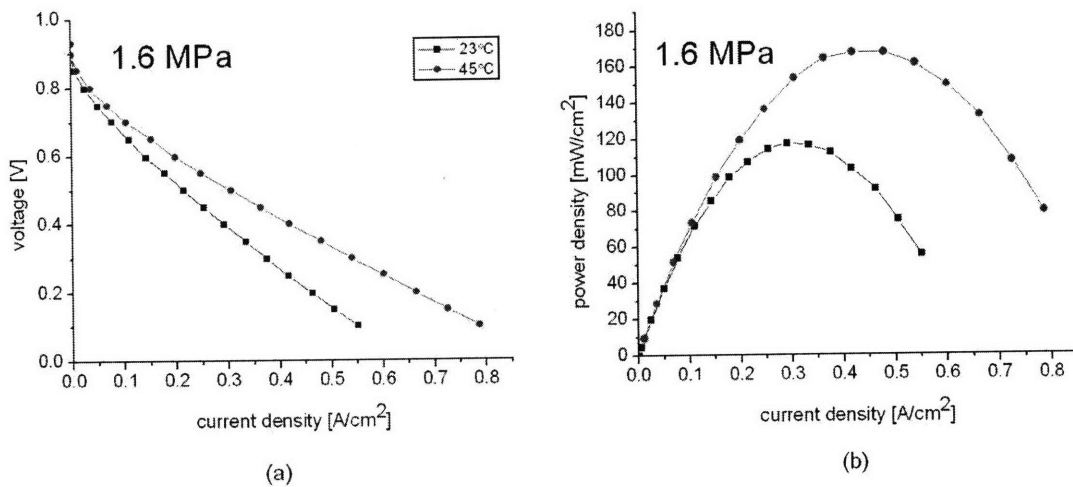


**Figure 32. Effect of cell temperature on (a) voltage-current and (b) the power-current curves at 1.6 MPa applied stress for a cell operating at 0 psi backpressure. Flow rates: 90 cc/min anode, 75 cc/min cathode. 100% relative humidity of inlet gases.**

When the applied stress was increased to 4.0 MPa, the current densities at both temperatures improved by 25-40% compared to room temperature performance, as shown in Figure 33a. As in the previous case, increasing the cell temperature caused both the kinetic and ohmic losses to decrease, and the peak power density increased from 166 W/cm<sup>2</sup> to 213 W/cm<sup>2</sup>, a net gain of 28% (Figure 33b). The percentage increase in power density due to increasing the cell temperature at constant stress was higher at 1.6 MPa than at 4.0 MPa, however, the absolute peak power density was on average 35% higher at 45°C than for room temperature operation.

A summary of the stress-performance relationship for different cell temperatures appears in Figure 34. The shape of these curves suggests that as a rule of thumb, performance can be improved at either temperature by increasing the applied stress, although the improvements in performance that are possible may be limited at stress higher than 4.0 MPa. It is expected that a cell temperature higher than 45°C should yield even better performance than what was shown here, since the kinetics would continue to improve with increasing temperature. However, an attempt to demonstrate this relationship experimentally yielded unexpected results; for further information and discussion, please refer to Appendix B.

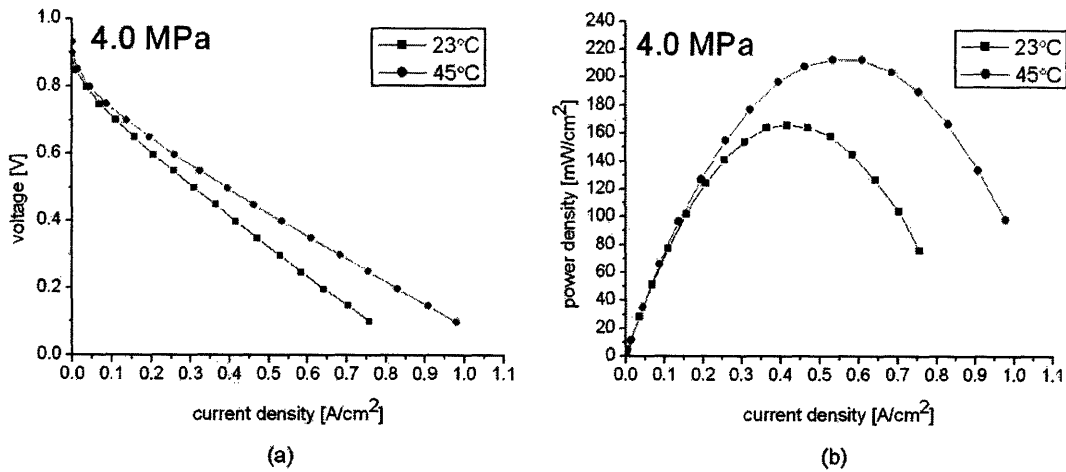


**Figure 33. Effect of cell temperature on (a) voltage-current and (b) the power-current curves at 4.0 MPa applied stress for a cell operating at 0 psi backpressure. Flow rates: 90 cc/min anode, 75 cc/min cathode. 100% relative humidity of inlet gases.**

#### *Voltage at Which Peak Power Occurred*

For the range of cell temperatures explored in this work, the peak cell performance occurred between 0.35-0.4 V (Figure 35), similar to what was observed previously for different inlet gas pressures. As before, the shape of the P-V curve changed significantly and a function of applied stress, with a flatter curve at 0.8 MPa and a much steeper curve occurring at 4.0 MPa. Since this behavior was observed for a variety of different operating conditions, it is likely that the changes in shape of the P-I curves truly result from changes in applied stress rather than the operating conditions chosen for the particular test.

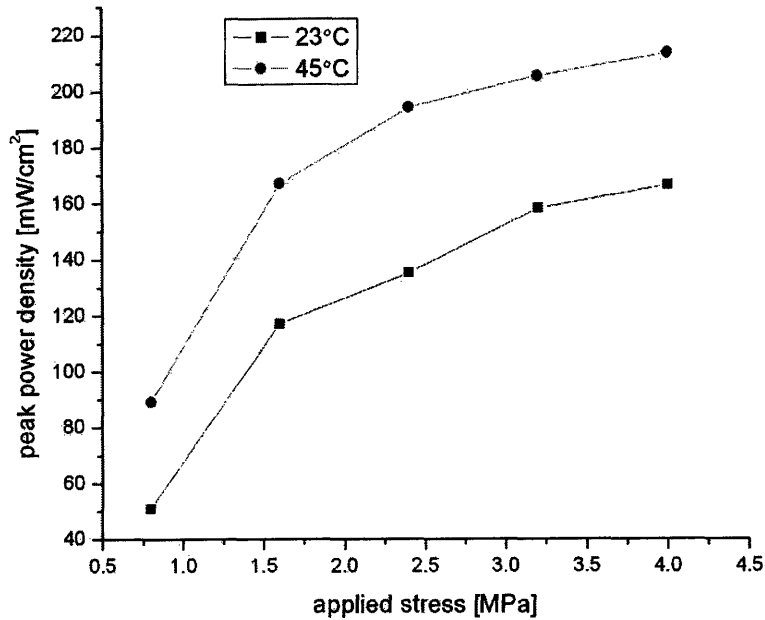


**Figure 34. Effect of cell temperature on the peak power density as a function of applied electrode stress.**

#### **5.4 Ohmic Resistance as a Function of Stress**

To get a sense for how the cell resistance changes as a function of applied stress, the slope of each V-I curve was measured by fitting a best-fit line to the linear regime. It should be noted that this is only an approximation since what appears to be a linear, “ohmic” relationship may actually conceal combined effects of activation and mass transport losses. Still, for a cell operating at low temperature, it can be assumed that the mass transport losses are small and that the performance is mostly dominated by ohmic losses at mid-to-low voltages.

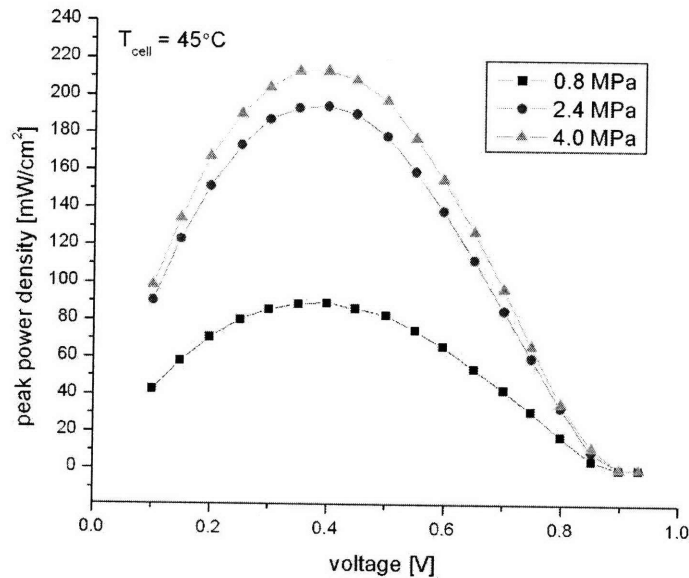


**Figure 35. Power density as a function of voltage and applied stress for a cell operating at 45°C and 0 psi gas backpressure. Flow rates: 90 cc/min anode, 75 cc/min cathode. 100% relative humidity of inlet gases.**

This analysis was performed for each of the V-I curves pertaining to the stress-backpressure data set. The result is shown in Figure 36. At 0.8 MPa, there is large variance among the calculated resistances. As stress increased, the resistance decreased exponentially and approached the same value of about 0.15  $\Omega$  for all backpressures. This performance agrees well with data presented in the literature on the contact resistance as a function of applied stress (Section 2.2.1) and confirms the hypothesis that changes in contact resistance dominate the resistance behavior at low applied stress.

### 5.5 Performance Optimization

The data presented in Sections 5.1-5.3 were used to generate 3D plots that describe how peak performance changes as a function of both applied stress and either backpressure (Figure 37) or temperature (Figure 38). These plots are very instructive for fuel cell design and optimization because they capture the inherent coupling between independent parameters and clearly demonstrate which parameters most significantly affect performance. For instance, it is clear from Figure 37 and Figure 38 that compressive



stress affects the power density more significantly than either cell temperature or backpressure for the variable ranges explored here, and that for a given stress, the power density is more dependent on changes in temperature than on changes in backpressure. These surfaces can help identify unexpected wells or peaks in the power density surface that result from parameter coupling and which may not be predictable by more traditional studies of individual fuel cell component behaviors.

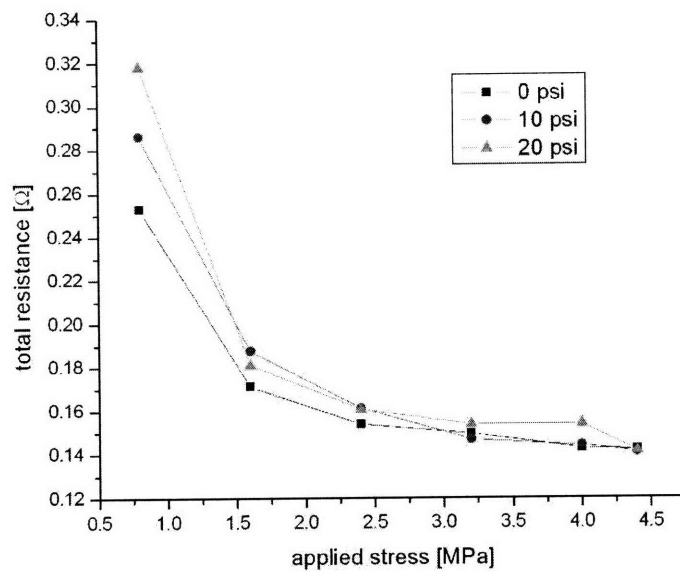


**Figure 36.** Cell ohmic resistance as a function of applied stress for a cell operating at room temperature (23°C) and different inlet gas backpressures. The ohmic resistance was obtained by fitting a line to the linear region of each V-I corresponding curve of the form shown in Figure 25.

While 3D plots are visually helpful for communicating the relationship between two independent parameters, this concept can be extended to multiple dimensions. By combining performance data for  $n$  independent parameters, an  $n+1$ -dimensional surface can be constructed. By numerically “walking” along this surface, ideal combinations of independent parameters could be identified. A fuel cell design engineer could then use this “library” of ideal parameter sets to design an optimally-performing cell that best meets a particular set of design constraints.

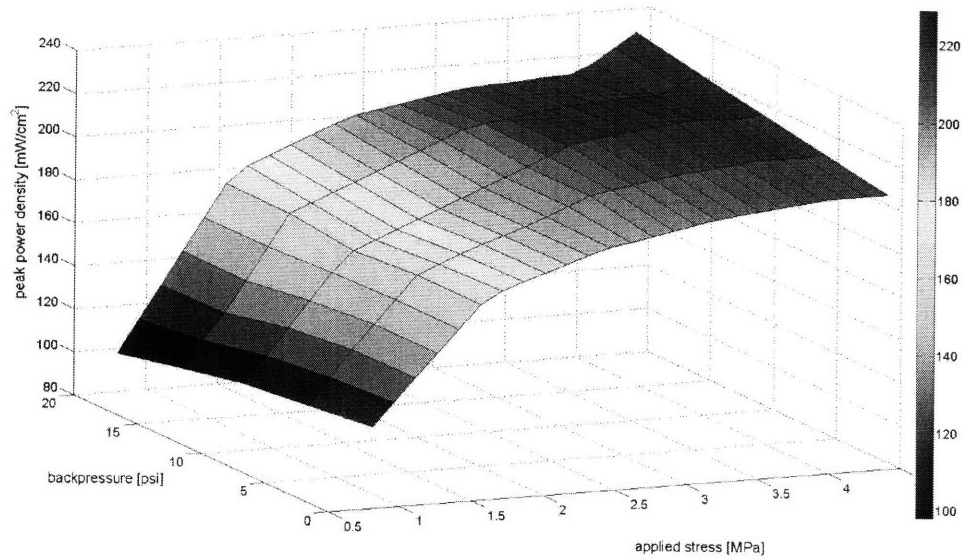


Figure 37. Peak power density as a function of backpressure and applied stress.

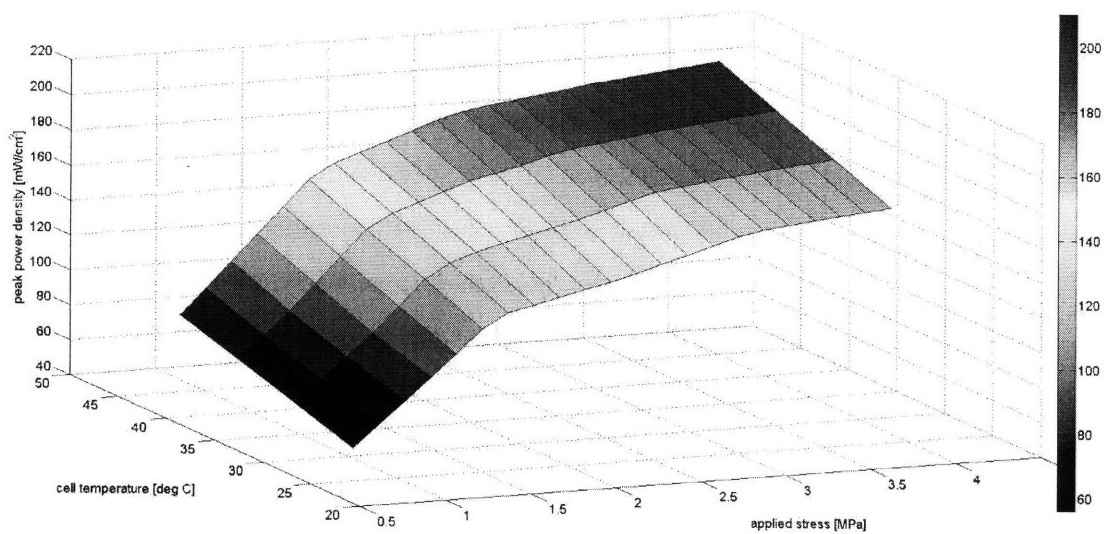


Figure 38. Peak power density as a function of cell temperature and applied stress.

## 5.6 Use of EIS to Support Findings

In order to support the above findings, and to provide another perspective on how applied stress affects performance, electrochemical impedance was performed for the cell

operating at 65°C and atmospheric pressure. Figure 39 depicts a typical impedance response obtained from the author's fuel cell setup under the given conditions and at 1.6 MPa applied stress.

The impedance response at 1.6 MPa appears as a single large semi-circle, suggesting that the cathode kinetic losses are much more significant in this cell than the anode kinetic losses. At low frequency, the “tail” feature that typically indicates mass transport resistance is absent; however, it is cautioned that due to very high noise sensitivity of the measurement equipment at low frequency, the data in the low-frequency regime may not reveal what is truly happening in the cell. At low voltage offset (high cell voltage), it is likely that mass transport is not an issue, and should therefore not feature in the AC impedance response anyway.

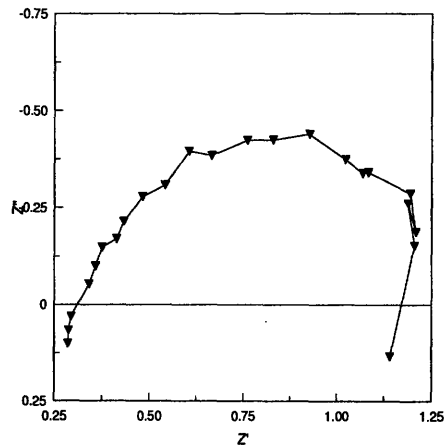


**Figure 39.** Impedance response for a cell operating at 65°C and 0 psi backpressure under 1.6 MPa applied electrode stress. The high-frequency real-axis intercept (at small  $Z'$ ) corresponds to the cell ohmic resistance, and the size of the semi-circle reflects the extent of kinetic losses at the electrodes.

The high-frequency intercept indicates that the total cell ohmic resistance was 0.3 Ω. This is roughly 80% larger than the value of 0.17 Ω measured in Section 5.4 for 1.6 MPa applied stress at room temperature and no backpressure. It is expected that increasing the cell operating temperature should improve the conductivity of Nafion and that the ohmic resistance measured with EIS should therefore be lower, not higher. A possible explanation for the higher ohmic resistance is that the EIS technique requires a different set of electrical leads to be connected to the cell, and this particular set of leads

was not necessarily optimized to reduce ohmic resistance like the leads that were used during all other cell testing. This increase in total ohmic resistance may therefore reflect differences in hardware rather than a change in chemical or mechanical properties of the MEA with temperature.

It may also be that the procedure outlined in Section 5.4 of fitting a slope to the linear region of the V-I curves might not accurately capture the true ohmic resistance, and perhaps the assumption of pure ohmic behavior in the mid-voltage regime is not valid. Still, the technique provides a rough estimate of how ohmic resistance changes with stress and is useful for starting to think about the various component resistances that contribute to the measured lumped resistance.

Figure 40 shows the effect of increasing the applied stress from 1.6 to 4.0 MPa at DC offset (overpotential) of 0.8 V (roughly 0.4 V cell voltage). As expected, the high-frequency intercept shifted to the left, indicating that the ohmic resistance decreased from 0.3 V to 0.25 V as a result of compression. Interestingly, the size of the semi-circle appeared to shrink with increasing stress, suggesting that the faradaic resistance due to kinetic limitations was reduced at higher compression. Although it is uncertain why the kinetics should be affected by mechanical compression, one possible explanation is that compression of the gas diffusion layer to high stress values brings the distributed catalyst particles into better electrical contact with the current collector. This model might help account for why peak performance reached a plateau, rather than declined, at very high stress – enhanced kinetics might help mitigate the effect of decreasing porosity and push the “degradation regime” to a higher stress range.

The effect of changing the cell voltage at a fixed applied stress of 1.6 MPa is shown in Figure 41. All three curves agree at high frequency and show the same high-frequency intercept, confirming that, as expected, the cell ohmic resistance did not change as a function of operating voltage. As the DC voltage offset decreased (cell voltage increased), the semi-circle grew in size. This agrees well with the AC impedance model of O’Hayre et al. [41]; at higher cell voltages, the driving force for cell kinetics (overpotential) is lower and the reaction kinetics at the electrodes are slower, resulting in a higher faradaic resistance as evidenced by a larger semi-circle diameter.

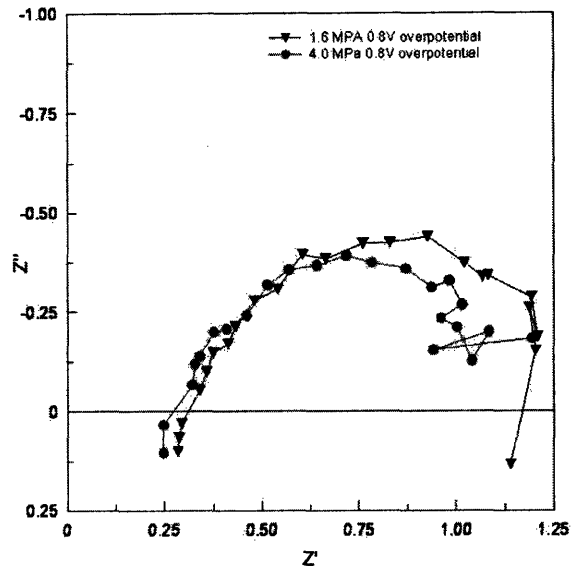


**Figure 40.** Effect of increasing applied electrode stress from 1.6 MPa to 4.0 MPa for a cell operating at 65°C and no backpressure. The ohmic resistance (high-frequency intercept) decreases from 0.30Ω to 0.25 Ω and the semi-circle diameter decreases.

A similar trend was observed as a function of operating voltage for an applied stress of 4.0 MPa, as shown in Figure 42, although the high-frequency intercept of all three curves shifted to the left by 0.05 V. As before, the semi-circle diameter decreased significantly from 1.6 to 4.0 MPa for all operating voltages. This again supports the idea that compression positively influences the electrode kinetics, a possibility which has not received much attention in the literature to date and which suggests a possible direction of future research.

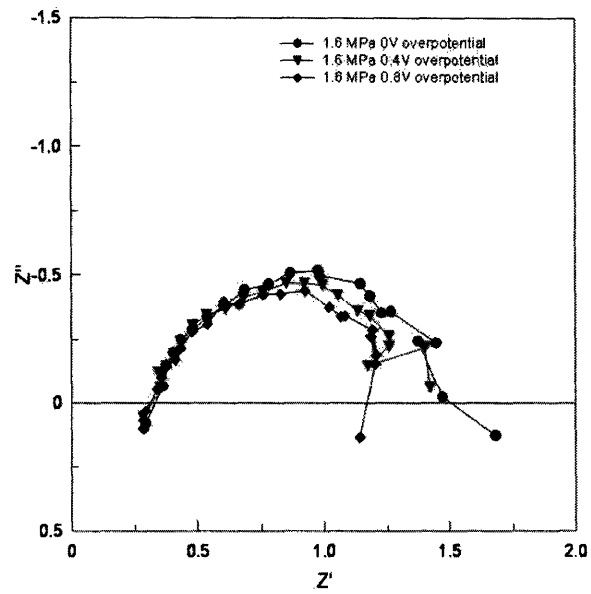


Figure 41. Effect of changing the cell voltage (overpotential) on the impedance response at 1.6 MPa.

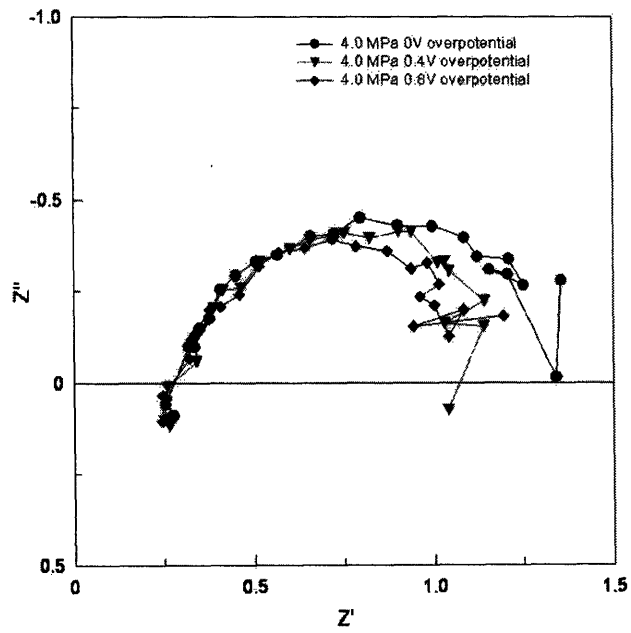


Figure 42. Effect of changing the cell voltage (overpotential) on the impedance response at 4.0 MPa.

## 6.0 Summary

This work presents the design and implementation of a novel test setup for studying the effect of electrode area compression on PEM fuel cell performance. While it is well accepted that applied stress is an important parameter for fuel cell design and optimization, a clear and accurate method of quantifying the stress-performance relationship has yet to emerge in the literature. The test setup presented here takes a unique approach to studying electrode compression that effectively decouples contact stress from sealing requirements and allows the applied electrode stress to be directly and accurately measured.

In general, the peak power density increased monotonically with applied stress for all operating conditions, with the largest gains at low stress magnitude (0.8 – 2.4 MPa). As stress increased beyond 4.0 MPa, the peak power density leveled off and there was no advantage in increasing applied stress further. This behavior at high stress is contrary to some of the results in the literature which show a peak in power density occurring at roughly 1-2 MPa and suggests that MEAs may be able to tolerate higher stresses than previously thought. Although it was not explored in this work, it is likely that there exists a stress magnitude larger than 4.4 MPa beyond which the power density would start to decline as a result of mechanical degradation. Overall, the power density increased by a factor of 2-3 over the range 0.8 to 4.0 MPa for all test conditions.

The effect of changing the operating conditions on fuel cell performance was explored at electrode stresses ranging from 0.8 MPa to 4.4 MPa for three different backpressures (0 psi, 10 psi and 20 psi) and three cell operating temperatures (23°C, 45°C and 65°C). At 0.8 MPa, increasing the backpressure from 0 psi to 20 psi caused the peak power density to decline monotonically, however, at 4.0 MPa, 10 psi gave optimal performance, followed by 20 psi. Increasing the cell temperature from 23°C to 45°C caused peak power to increase by roughly 50 mW/cm<sup>2</sup> for all magnitudes of stress. Nominally, the results suggest that it is always better to operate at higher stress, higher temperature and, for the most part, at higher backpressure; however, significant performance tradeoffs associated with operating in these “extreme” regimes were identified and discussed.

At low stress magnitudes, the shape of the power-voltage (P-V) curve was flat near peak power; however, as applied stress increased, the shape of the curves became increasingly sharper for all operating conditions. This suggests that selection of operating voltage is less critical at lower stress, since power can be optimized for a wider range of voltages. However, selection of operating voltage is much more critical at high stress since performance declines more steeply around the peak.

The author's test setup enables a new method for optimizing fuel cell performance that identifies which parameters can yield the greatest improvements in power. For example, at 2.4 MPa, it is more useful to increase the cell temperature from 23°C to 45°C (for a gain in power density of 52%) rather than increase the backpressure to 20 psi (a gain in power density of only 7%). Additionally, for the range of stress explored here, it is much more effective to increase the electrode stress than to change either of the other two operating conditions.

Two methods for measuring the ohmic resistance of the cell were discussed. The first, which involves fitting a slope to the V-I curves, is useful for visualizing how resistance changes with compression and agrees well with the general form of contact resistance data presented in the literature. Electrochemical impedance spectroscopy was used to measure both ohmic resistance and the activation losses at the electrodes as a function of applied stress.

Overall, this test setup allows for electrode stress to be rigorously considered as an important parameter that affects the fuel cell performance. Once the performance as a function of stress and other operating conditions is fully quantified and understood, this knowledge can be used to drive next-generation fuel cell designs with improved power capabilities.



## 7.0 Future Work and Impact

So far, the effect of changing two operating parameters (inlet gas pressure and cell temperature) on the stress-performance relationship has been explored for one particular cell configuration. In the immediate future, this work could be expanded to include the effect of changing additional operating parameters such as inlet gas relative humidity, gas flow stoichiometry, and gas flow rates. Following the procedure outlined in this paper, this data could be combined to paint a more complete picture of fuel cell performance that would consider the coupled effect of electrode stress and other operating parameters for perhaps the first time.

In addition to studying the effect of operating conditions on fuel cell performance, future work will address how the stress-performance relationship depends on the engineering parameters used to design and construct the cell. As a simple first step, a variety of different membrane and GDE combinations could replace the current MEA that was used for all the studies presented in this paper. Additionally, a variety of new Adjustable Current Collectors (ACC) could be manufactured from various different materials, including graphite and nickel alloys, and having different flow field geometries. The use of various ACCs could help illuminate the dependence of the stress-performance relationship on material property and current collector morphology, and may help indicate optimal designs for a given applied stress. Since the ACC is a modular component of the fuel cell test setup, it is straightforward to replace the current stainless steel ACC with newly manufactured alternatives.

It would be useful in future research to use this test setup to gain a better understanding of the resistance contributions in the cell. For instance, electrochemical impedance data obtained using this test setup could be combined with targeted studies of membrane conductivity and interfacial resistance as a function of applied stress in order to quantify how each component resistance contributes to the bulk resistance as a function of stress. Knowledge obtained from this experiment could identify the significant ohmic loss contributions in the cell as a function of stress and help suggest methods for reducing this loss.

### *Improvement of the Current Setup*

The current setup has been successful as a proof-of-concept for accurately applying and measuring decoupled compressive stress to the electrode area of a PEM fuel cell. However, the setup could be improved in a number of ways that will improve data collection and interpretation. For instance, the current method of force actuation (using a compression spring) is limited in both accuracy and precision. While this has sufficed for the current study, an improved design would feature an electronic force actuator that would help remove some of the measurement uncertainty. Additionally, the o-ring interface between ACC and the top outer plate could be revisited in order to further reduce the friction and improve the measurement accuracy of the applied stress.

### *Development of a Stress Sensing Device*

The state of stress in the membrane during operation is interesting to fuel cell researchers and designers because it can affect the long-term mechanical and chemical stability of the cell. However, to date it has been difficult to accurately measure the stress state *in-situ*. Rather than using the ACC to *apply* stress to the electrode and membrane, the concept of this translational, decoupled component could be extended to a precision device in which the membrane stress is *measured* for different operating conditions. This would allow researchers to accurately monitor the evolution of stress in the membrane while circumventing traditional sealing concerns, which have complicated *in-situ* stress measurements in the past.

### *Commercial Applications*

The test apparatus presented in this work could be attractive to fuel cell companies that desire a more quantitative, accurate way of anticipating the effect of clamping pressure on their product's performance. Clamping force is widely regarded in industry as being significant but the approach to measuring and optimizing it has so far required a great deal of trial-and-error. The test apparatus would provide fuel cell developers with a tool that indicates which parameters should receive the most attention for maximizing power output, helping to reduce the amount of costly and time-consuming testing that is required for product development.

Companies that specialize in the manufacture of fuel cell components could use this apparatus to drive the design of components that have properties tailored to be optimal at a given stress. For instance, gas-diffusion media could be developed that have higher stiffness at optimal stress so that the performance degradation due to decreasing porosity can be averted or shifted beyond the operating stress range. Additionally, new fuel cell systems could be designed in order to target and reduce the large contact resistance between materials at low applied stress by mechanically integrating components such as the current collector and electrode structure.

Finally, the concept of decoupled electrode stress application could be implemented as a next-generation fuel cell design in which varying amounts of force are applied depending on the operating conditions. This could be accomplished using an electronic force actuator integrated with an optimal control system that would constantly monitor fuel cell performance and optimize it *in-situ*. Rather than operate under constant, pre-determined operating conditions, the control system could instead vary parameters during operation to address any unforeseen changes in performances that often arise during fuel cell testing. This concept of a dynamic-force fuel cell is novel and deviates from traditional designs in which the fuel cell, and its stress state, is fixed prior to operation.

# Bibliography

- [1] "Fuel Cell Origins: 1840-1890." Smithsonian Institution, 2004.  
<http://americanhistory.si.edu/fuelcells/origins/origins.htm>
- [2] Grimwood, J. M., Hacker, B.C. and Vorzimmer, P.J., "Project Gemini: Technology and Operations." NASA Report: The NASA Historical Series, 1969. Available at [http://ntrs.nasa.gov/archive/nasa/casi.ntrs.nasa.gov/19690027123\\_1969027123.pdf](http://ntrs.nasa.gov/archive/nasa/casi.ntrs.nasa.gov/19690027123_1969027123.pdf).
- [3] Larminie, J., Dicks, A., "Fuel Cell Systems Explained," John Wiley & Sons, 2003. Available online at <http://www.knovel.com>.
- [4] "Hydrogen Cars," <http://www.hydrogencarsnow.com>.
- [5] Robertson, D., "Boeing tests first hydrogen powered plane," Times Online, April 03, 2008. [http://business.timesonline.co.uk/tol/business/industry\\_sectors/transport/article3675188.ece](http://business.timesonline.co.uk/tol/business/industry_sectors/transport/article3675188.ece).
- [6] Bossel, U., Does a Hydrogen Economy Make Sense?, Proceedings of the IEEE 94 (2006). Available online at <http://www.efcf.com/reports/E21.pdf>.
- [7] Romm, Joseph, *The Hype About Hydrogen: Fact and Fiction in the Race to Save the Climate*, Island Press, 2004.
- [8] *The Hydrogen Economy: Opportunities, Costs, Barriers, and R&D Needs*, National Academy of Engineering Board on Energy and Environmental Systems, The National Academies Press, 2004.
- [9] Blencoe, G. and J., "Hydrogen: Fuel of the Future," Hydrogen Discoveries, Inc. Available online at <http://www.hydrogendiscoveries.com/vision.html>.
- [10] van Dokkum, J., Dasinger, A., Meeting the challenges in the transport sector, J. Power Sources, Received November 06 2007. In Press.
- [11] DOE Report: *Hydrogen, Fuel Cells and Infrastructure Technologies Program's Multi-Year Research, Development and Demonstration Plan*, October 2007, available online at [http://www1.eere.energy.gov/hydrogenandfuelcells/mypp/pdfs/fuel\\_cells.pdf](http://www1.eere.energy.gov/hydrogenandfuelcells/mypp/pdfs/fuel_cells.pdf).
- [12] "World record for fuel cell buses," <http://www2.mercedes-benz.co.uk>, 2005.
- [13] Ballard "Road Map." Summary available online at <http://www.fuelcellworks.com/Suppage2336.html>.

- [14] Matsumoto, M., Usami, K., PAFC Commercialization and Recent Progress of Technology in Mitsubishi Electric, in *The International Fuel Cell Conference Proceedings*, NEDO/MITI, Tokyo, Japan, 1992.
- [15] "Fuel Cell Handbook, 5th Edition", Report prepared by EG&G Services, Parsons, Inc. and Science Applications International Corporation under contract no. DE-AM26-99FT40575 for the U.S. Department of Energy, National Energy Technology Laboratory, October 2000.
- [16] Eric L. Thompson, *Electron Microscope Analysis of Low Temperature Damage in PEM Fuel Cells*, Department of Chemical Engineering, University of Rochester. <http://www.optics.rochester.edu/workgroups/cml/opt307/spr05/eric/>
- [17] <http://www.fuelcellstore.com>
- [18] Tawfik, H., Hung, Y., Mahajan, D., Metal bipolar plates for PEM fuel cell – A review, *J. Power Sources* **163** (2007) 755-767.
- [19] Silva, R.F., Franchi, D., Leone, A., Pilloni, A., Masci, A., Pozio, A., Surface conductivity and stability of metallic bipolar plate materials for polymer electrolyte fuel cells, *Electrochimica Acta* **51** (2006) 3592-3598.
- [20] <http://www.hokuscientific.com/images/diagram.gif>
- [21] Vanysek, Petr (2006). "Electrochemical Series," in *Handbook of Chemistry and Physics: 87<sup>th</sup> Edition* (Chemical Rubber Company).
- [22] *Thermophysical Properties of Fluid Systems*, National Institute of Standards and Technology. Available online at <http://webbook.nist.gov/chemistry/fluid/>
- [23] Slade, S., Campbell, S. A., Ralph, T.R., and Walsh, F.C., Ionic Conductivity of an Extruded Nafion 1100 EW Series of Membranes, *J. Electrochemical Society* **149** (2002) A1556-A1564.
- [24] Liu, D., Hickner, M. A., Case, S.W., Lesko, J.J., Relaxation of Proton Conductivity and Stress in Proton Exchange Membranes Under Strain, *J. Engineering Materials and Technology* **128** (2006) 503.
- [25] Yan, W.-M., Chen, C.-Y., Mei, S.-C., Soong, C.-Y., Chen, F., *J. Power Sources* **162** (2006) 1157-1164.
- [26] Kumar, A., Reddy, R., Effect of channel dimensions and shape in the flow-field distributor on the performance of polymer electrolyte membrane fuel cells, *J. Power Sources* **113** (2003) 11-18.

- [27] Mishra, V., Yang, F., Pitchumani, R., Measurement and prediction of electrical contact resistance between gas diffusion layers and bipolar plate for application to PEM fuel cells, *Transactions of the ASME: Journal of Fuel Cell Science and Technology* **1** (2003) 2-9.
- [28] Wang, G., Sweikart, M.A., Turner, J.A., Stainless steel as bipolar plate material for polymer electrolyte membrane fuel cells, *J. Power Sources* **115** (2003) 243-251.
- [29] Zhou, P., Wu, C.W., Ma, G.J., Contact resistance prediction and structure optimization of bipolar plates, *J. Power Sources* **159** (2006) 1115-1122.
- [30] Bazylak, A., Sinton, D., Liu, Z.-S., Djilali, N., Effect of compression on liquid water transport and microstructure of PEMFC gas diffusion layers, *J. Power Sources* **163** (2007) 784-792.
- [31] Ge, J., Higier, A., Liu, H., Effect of gas diffusion layer compression on PEM fuel cell performance, *J. Power Sources* **159** (2006) 922-927.
- [32] Ihonen, J., Mikkola, M., Lindbergh, G., Flooding of gas diffusion backing in PEFCs, *J. Electrochemical Society* **151** (2004) A1152-A1161.
- [33] S. Escribano, J.-F. Blachot, J. Etheve, A. Morin, R. Mosdale, *J. Power Sources* **156** (2006) 8-13.
- [34] Zhou, P., Wu, C.W., Ma, G.J., Influence of clamping force on the performance of PEMFCs, *J. Power Sources* **163** (2007) 874-881.
- [35] Ous, T., Arcoumanis, C., Effect of compressive force on the performance of a proton exchange membrane fuel cell, *Proc. IMechE: J. Mechanical Engineering Science* **221C** (2007) 1067-1074.
- [36] Lee, W.-K., Ho, C.-H., Van Zee, J.W., Murthy, M., The effects of compression and gas diffusion layers on the performance of a PEM fuel cell, *J. Power Sources* **84** (1999) 45-51.
- [37] Chang, W.R., Hwang, J.J., Weng, F.B., Chan, S.H., Effect of clamping pressure on the performance of a PEM fuel cell, *J. Power Sources* **166** (2007) 149-154.
- [38] Fekrazad, N., Bergman, T.L., The effect of compressive load on proton exchange membrane fuel cell stack performance and behavior, *Transactions of the ASME: Journal of Heat Transfer* **129** (2007) 1004-1013.
- [39] Schmittinger, W., Vahidi, A., A review on the main parameters influencing long-term performance and durability of PEM fuel cells, *J. Power Sources* **180** (2008) 1-14.

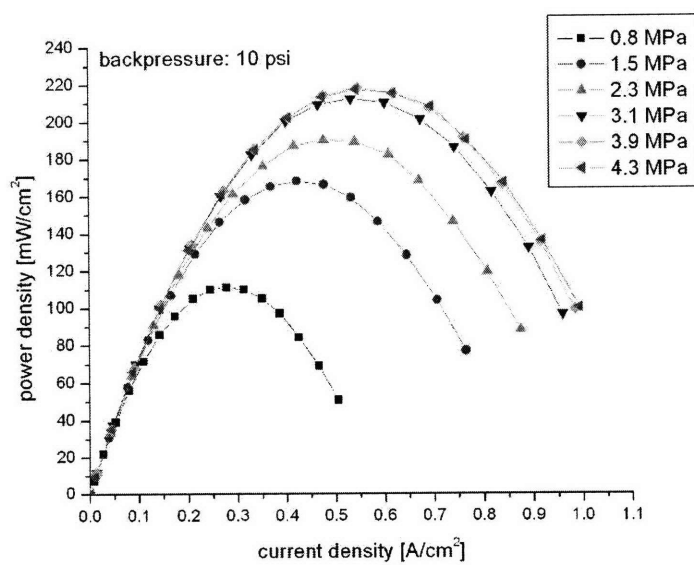
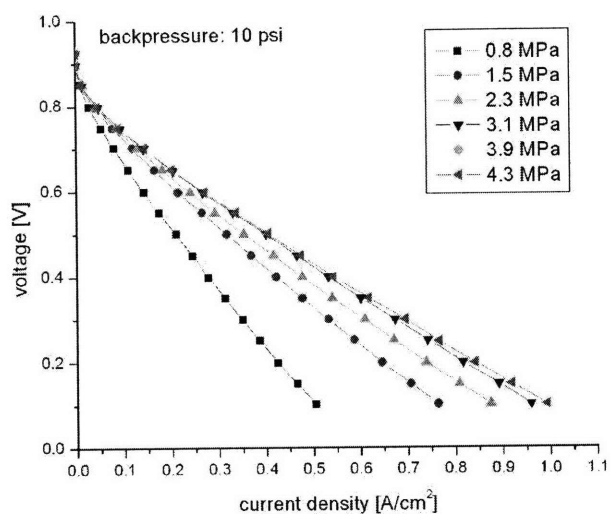
- [40] Scholta, J., Escher, G., et al., Investigation on the influence of channel geometries on PEMFC performance, *J. Power Sources* **155** (2006) 66-71.
- [41] O'Hayre, R., Cha, S.-W., Colella, W., Prinz, F., *Fuel Cell Fundamentals*. John Wiley & Sons: New York, 2006.
- [42] Springer, T.E., Zawodzinski, T.A., Wilson, M.S., Gottesfeld, S., Characterization of Polymer Electrolyte Fuel Cells Using AC Impedance Spectroscopy, *J. Electrochemical Society*, **143** (1996) 587-599.
- [43] Ciureanu, M., Roberge, R., Electrochemical Impedance Study of PEM Fuel Cells. Experimental Diagnostics and Modeling of Air Cathodes. *J. Physical Chemistry* **105** (2001) 3531-3539.
- [44] Cahan, B.D., Wainright, J.S., AC Impedance Investigations of Proton Conduction in Nafion, *J. Electrochem Society* **140** (1993) L185..
- [45] Gruber, D., Muller, J., *J. Power Sources* **27** (2007) 294-301.
- [46] Qi, Z., Kaufman, A., *J. Power Sources* **111** (2002) 181-184.

## Appendix A: Additional Stress-Performance Data

V-I and P-I curves as a function of stress are presented here for different sets of operating conditions:

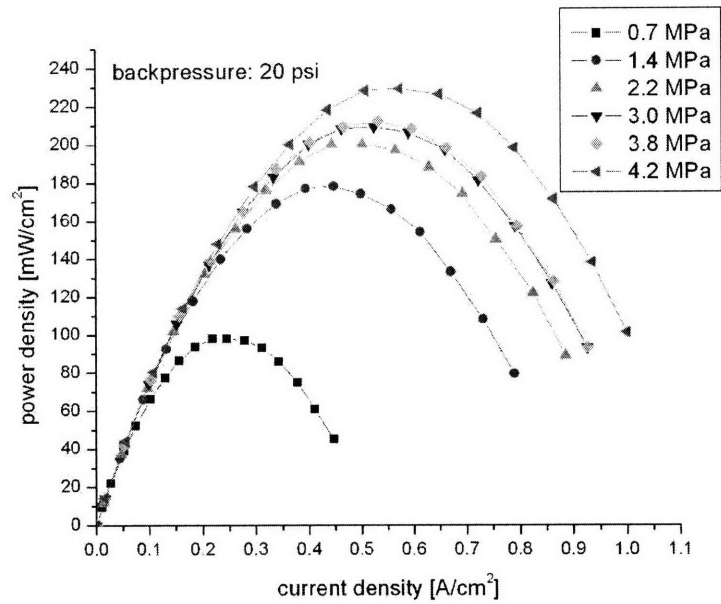
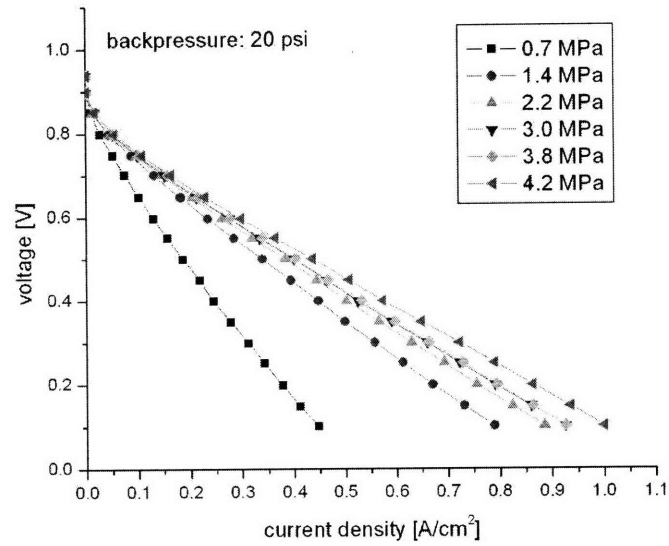
### *Backpressure Effect*

- Cell temperature: 23°C; Backpressure: 10 psi; Flow rates: 90 cc/min anode, 70 cc/min cathode; Relative humidity: 100%



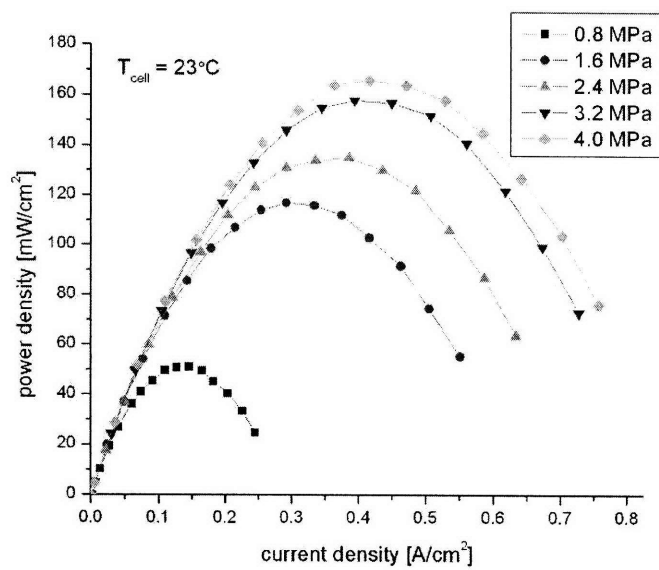
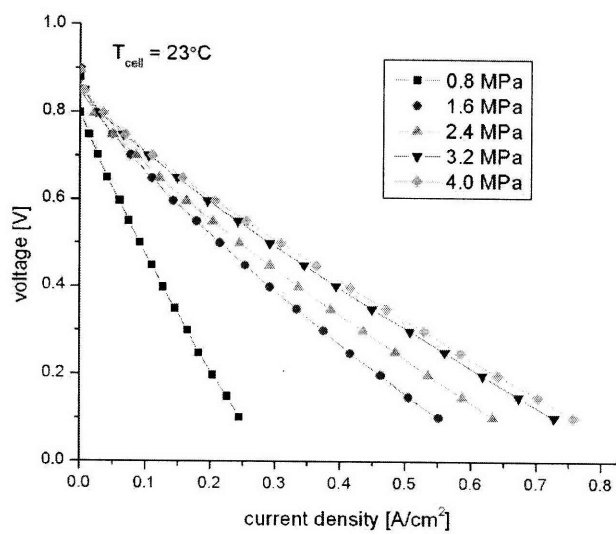


- Cell temperature: 23°C; Backpressure: 20 psi; Flow rates: 90 cc/min anode, 70 cc/min cathode; Relative humidity: 100%

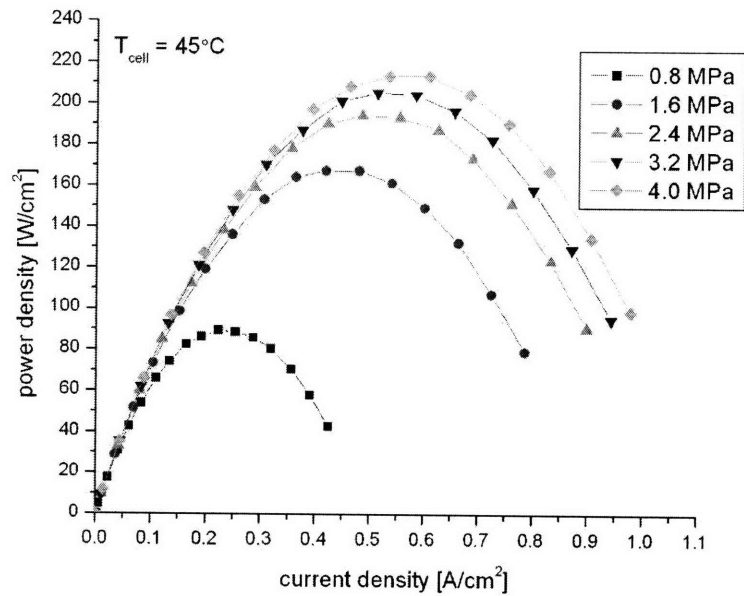
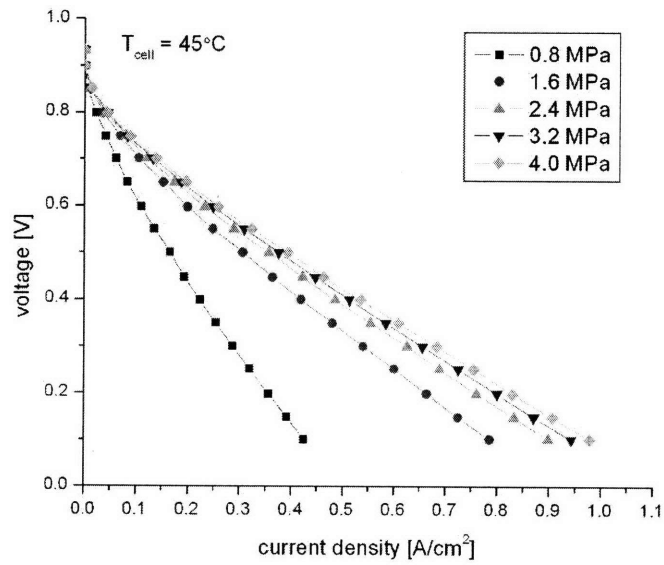


### Temperature Effect

- Cell temperature: 23°C; Backpressure: 0 psi; Flow rates: 90 cc/min anode, 70 cc/min cathode; Relative humidity: 100%



- Cell temperature: 45°C; Backpressure: 0 psi; Flow rates: 90 cc/min anode, 70 cc/min cathode; Relative humidity: 100%



## Appendix B: Effect of Cell Operation at 65°C

According to the discussion in Section 2.1.7, increasing the cell operating temperature should improve the electrode kinetics and therefore the performance at all current densities. However, the cell performance at 65°C was intermediate between 23°C and 45°C. A comparison of V-I and P-I curves at the three temperatures and 1.6 MPa are shown in Figure 43a and Figure 43b, respectively. The corresponding stress-power curves as a function of temperature, as well as the 3-D surface plot of power density, are shown in Figure 44 and Figure 45, respectively.

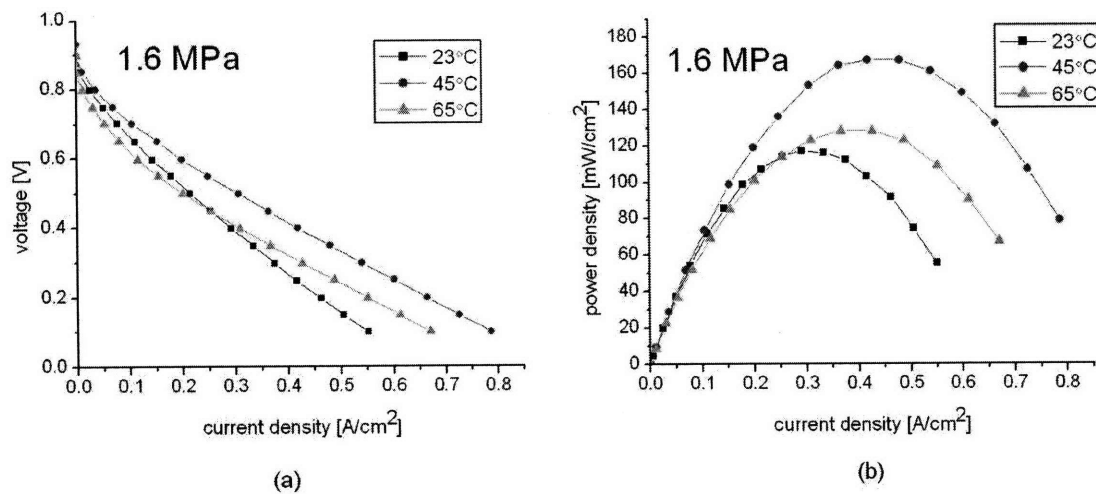


**Figure 43. Effect of cell temperature on (a) V-I and (b) P-I curves at 1.6 MPa applied stress. Increasing from 23°C to 45°C improves the performance, however, further increasing the temperature to 65°C causes a decline in performance. The large activation losses for the 65°C curve suggest that water may have collected in the cell and blocked the catalyst sites, effectively decreasing the catalyst surface area.**

The voltage drop-off due to kinetic limitations at low current densities is much more severe at 65°C than for the other two operating conditions. The reason for this is unclear, since increased temperature usually helps the kinetics. One possibility is that during cell conditioning at 65°C, the cell became flooded and remained that way throughout all the tests at that condition. Water that is trapped in the electrode can prevent oxygen and hydrogen from accessing the catalyst sites; the result is an effective reduction in catalyst surface area, which has a drastic effect on the cell kinetics. It is

interesting that at high current densities, the slope of the 65°C curve appears to equal that of the 45°C curve, which suggests that the ohmic resistance is the same in both cases.

It is possible that the inability to manage water well at higher cell temperatures is inherent to the particular fuel cell design used in this work, and that the expected monotonic increase in cell performance with temperature would be observed if the cell were redesigned to reduce flooding near the catalyst layer. If this limitation were successfully removed, a number of interesting temperature-dependent features of fuel cell performance could be studied. For instance, in all of the results presented in this paper, the peak power consistently occurred at 0.4 V, regardless of the applied stress. The optimal cell voltage is determined by the shape of the V-I curve at high current density and is affected by both ohmic losses and mass transport limitations. An improved cell with large current generation would be more susceptible to mass transport losses at high temperature and in the vicinity of 0.4 V than the current setup. The result could be a rapid drop-off in the power density at low current, and a shift of the peak power to a higher cell voltage. In this hypothetical case, since applied stress could also significantly affect the water management capabilities of the cell, the voltage at which peak power occurs could vary significantly depending on the operating conditions.

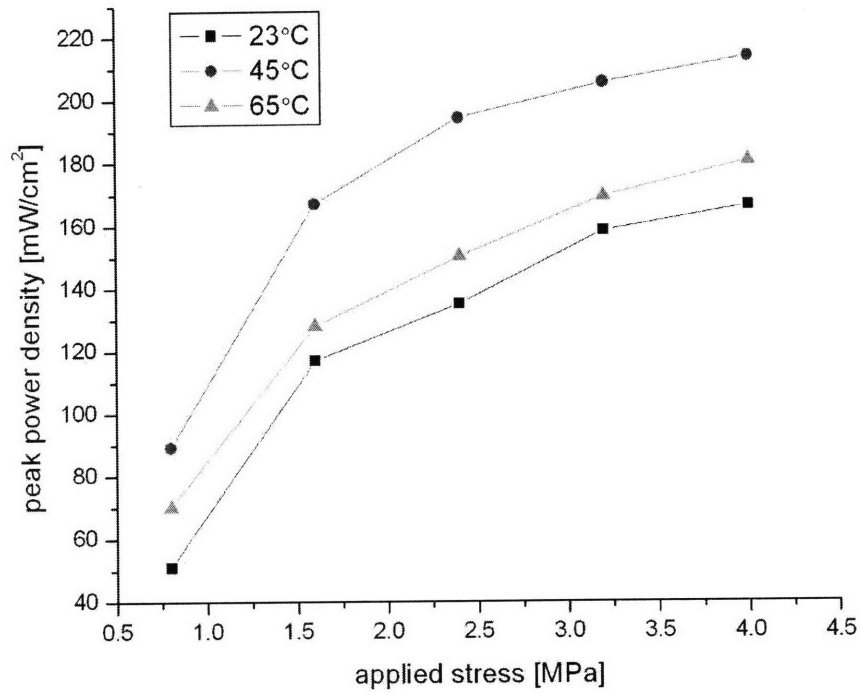


Figure 44. Peak power density as a function of cell temperature and applied electrode stress.

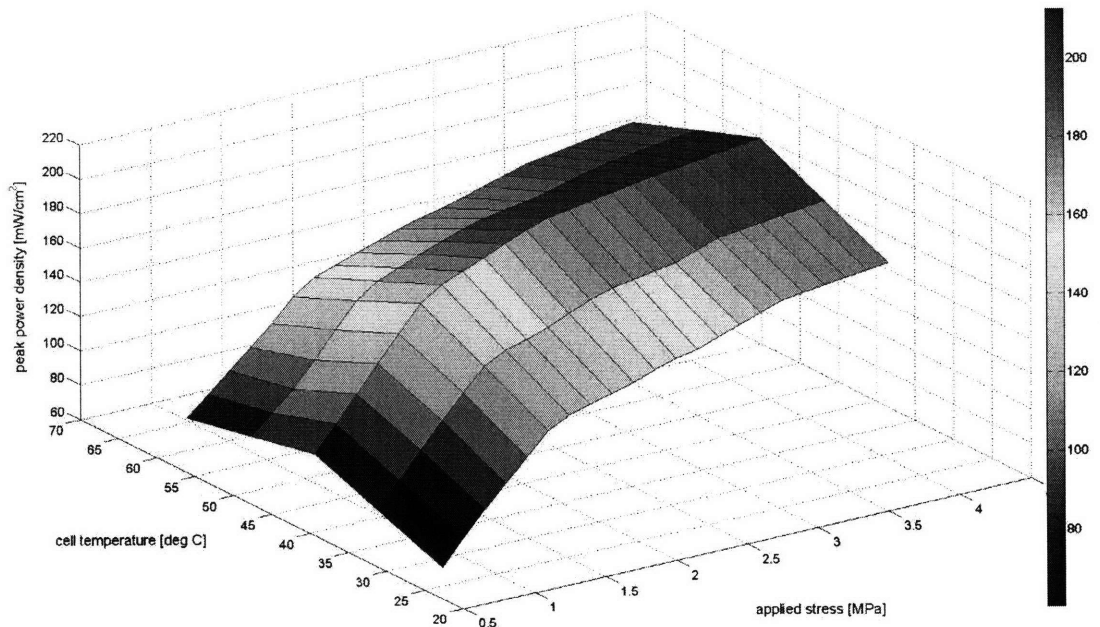


Figure 45. 3-D representation of the peak power dependency on cell temperature and applied stress.